Journal of Nanobiotechnology

RESEARCH

Open Access

3D printed shape-memory piezoelectric scaffolds with in-situ self-power properties for bone defect repair

Bing Li[1], Yichao Ma[2], Kanwal Fatima[1], Xiaojun Zhou[1], Xin Gu[3*], Shuo Chen[1,4*] and Chuanglong He[1*]

Abstract

Electrical stimulation has been shown to regulate early immunity and late-stage osteogenesis in bone repair. However, achieving in-situ electrical stimulation in the form of self-power in vivo during the initial postoperative stages when the patients have limited mobility remains challenging. In this study, we developed a 3D-printed in-situ self-powered composite scaffold composed of shape memory polyurethane elastomers (SMPU) and polyvinylidene fluoride (PVDF) piezoelectric nanofibers. The composite scaffold demonstrates excellent shape memory performance, allowing for minimally invasive implantation. During the shape memory process, the composite scaffold can provide mechanical force stimulation to PVDF nanofibers to generate charge. Therefore, self-power was achieved through the integration of the shape memory process and piezoelectric effects, and it can be used for in-situ electrical stimulation during the initial postoperative period. Additionally, the composite scaffold can output voltage under continuous mechanical force stimulation, indicating that the patients can apply sustained mechanical force stimulation to the composite scaffold to output voltage through rehabilitation exercises when the patients regain mobility. Both cell experiments and animal studies confirmed that this composite scaffold can effectively regulate the immune microenvironment and enhance osteogenesis. This study successfully achieves in-situ electrical stimulation in the form of self-power by integrating the shape memory process and piezoelectric effects, which is expected to be an effective repair strategy for bone tissue engineering.

Keywords Piezoelectric, Shape memory, Self-power, Bone repair

*Correspondence:
Xin Gu
guxin2004ty@163.com
Shuo Chen
schen@dhu.edu.cn
Chuanglong He
hcl@dhu.edu.cn
Full list of author information is available at the end of the article

Graphical Abstract

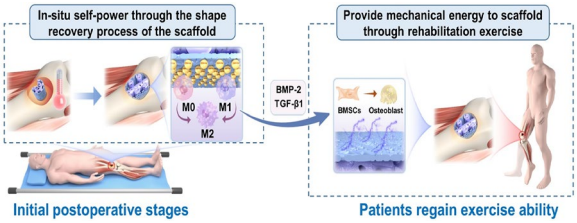

Introduction

Bone repair is a time-sequential process involving early-stage immune microenvironment modulation and late-stage osteogenesis [1, 2]. Studies have shown that electrical signals can effectively regulate immunity and promote osteogenesis [3–6]. However, achieving in-situ electrical stimulation in vivo remains a challenge. While implantable electrodes are widely used for in-situ electrical stimulation in bone repair, they require an external power source, complicating the treatment process [7]. Currently, the primary challenge in achieving in-situ electrical stimulation is enabling the electronic devices to apply electrical stimulation spontaneously without reliance on external devices. Consequently, there is increasing interest in intelligent electronic devices with stimulus-responsive properties. Triboelectric and piezoelectric materials can generate charge under mechanical force stimulation and are widely used in tissue engineering because they can provide electrical stimulation without the need for an external power source [8–10]. Shao et al. [11] used polycaprolactone (PCL) and PVDF as raw materials to fabricate an ultrasonic electromechanical treatment system for long-gap peripheral nerve repair using electrospinning technology. The nanofibers can output voltage under ultrasound stimulation to improve the proliferation and the expression of neurotrophic factors in Schwann cells, as well as the neuronal growth and differentiation of PC12 cells. In addition, linearly aligned nanofibers provide nanotopography-based contact guidance to further promote neurite outgrowth during regeneration. Hu et al. [12] fabricated PVDF nanofibers with random and aligned fiber orientations using electrospinning technology and further improved the piezoelectrical properties of nanofibers by high-temperature annealing. In this work, the authors demonstrated that the traction forces generated by cell adhesion and migration can induce the deformation of the nanofibers, trigger the piezoelectric effect of the nanofibers, and generate charge to stimulate the osteogenic differentiation of stem cells, realizing the self-triggering regulation of osteogenic differentiation by stem cells. Although the application of piezoelectric materials in tissue engineering has proved that they can generate electrical signals for tissue repair without an external power source, the source of mechanical force has become the main challenge of piezoelectric materials to apply electrical stimulation spontaneously without relying on external devices. Most studies have used medical ultrasound devices to provide mechanical stimulation, failing to achieve in-situ electrical stimulation without relying on external devices [13–16]. Although relevant studies have proved that the traction force generated by cell adhesion and migration can stimulate piezoelectric materials to produce electrical signals, whether the electrical signals generated by this method can meet the needs of tissue repair remains to be studied. Previous studies have applied mechanical force stimulation to triboelectric/piezoelectric electronic devices through rehabilitation exercises to achieve in-situ electrical stimulation [17]. However, this approach is limited because many patients lack the ability to exercise during the initial postoperative stages. Moreover, the structure of most previously reported triboelectric/piezoelectric electronic devices is primarily a complex two-dimensional structure, which poses challenges for minimally invasive implantation, and few of these devices have been applied in the form of scaffolds for bone defect repair [18–20]. You et al. successfully fabricated triboelectric scaffolds based on poly(glycerol sebacate) (PGS), poly(3,4-ethylenedioxythiophene) (PEDOT), and polystyrene sulfonate (PSS), which can achieve in-situ electrical stimulation through frictional contact during human exercise [21]. Unfortunately, these scaffolds are also unsuitable for use during the initial postoperative period due to the patient's limited exercise ability. Therefore, there is a critical need to develop minimally invasive implantable self-powered

bone tissue engineering scaffolds that can achieve time-sequential regulation of immune microenvironment and osteogenesis during bone repair.

Shape memory polymers (SMPs) can fix the temporary shape and recover the permanent shape under specific external stimuli, such as room temperature and physiological temperature. This phenomenon is referred to as the shape memory effect [22–25]. SMPs are particularly advantageous for bone repair applications due to their excellent minimally invasive implantation performance. The SMP scaffold with a temporary shape can be implanted through smaller incisions and recover to the original shape after implantation [22, 26]. Lai et al. [27] prepared a near-infrared-responsive shape-memory bone repair scaffold using shape-memory polyurethane and magnesium nanoparticles as raw materials. The scaffold can be compressed into a small size before implantation, which could be easily implanted into the defect site. After implantation, the scaffold can recover the original shape and completely fill the defect site under near-infrared light irradiation. Zhao et al. [25] prepared a photothermal-responsive shape memory bone tissue engineering scaffold (BP/peptide/TCP/P(DLLA-TMC)) by incorporating black phosphorus nanosheets and osteogenic peptide into β-tricalcium phosphate/poly(lactic acid-co-trimethylene carbonate) (TCP/P(DLLA-TMC)) nanocomposite scaffold. The scaffold can be compressed into a small size before implantation, which can be easily implanted into the defect site by minimally invasive surgery. After implantation, the scaffold's temperature can quickly increase to 45 ℃ and recover its original shape under near-infrared light irradiation. Due to the shape reconstruction property of the scaffold, the scaffold can fit the irregular bone defect boundary well. Additionally, the scaffold has sufficient compressive strength at physiological temperature to provide long-term mechanical support. Research has shown that the shape-recovery process of SMPs involves the release of mechanical energy [28]. By combining flexible piezoelectric materials with SMPs, it is possible to prepare composite scaffolds that can provide mechanical force stimulation to induce deformation in the piezoelectric materials during the shape-memory process. According to the literature, flexible piezoelectric materials such as PVDF can generate charge when they undergo deformation, such as bending by mechanical force stimulation [29]. Based on this strategy, the composite scaffold is expected to achieve in-situ self-power and be used to modulate the immune microenvironment during the initial postoperative period. Furthermore, bone tissue, particularly load-bearing bones, can experience compression during physical activity, resulting in mechanical force absorption and deformation [30]. Therefore, as treatment progresses, patients can apply sustained mechanical force stimulation to the composite scaffold through rehabilitation exercises when they regain exercise ability, enabling the composite scaffold to output voltage for bone repair. Despite this combined strategy's potential for bone defect repair, no similar designs have been reported to date.

In this study, we developed an in-situ self-powered composite scaffold composed of SMPU and PVDF using 3D printing and electrospinning technology (Fig. 1). The composite scaffold features a customized three-dimensional structure, can achieve structural and functional transformation at physiological temperatures, and has the ability for minimally invasive implantation. After undergoing a shape memory process, the composite scaffold can generate a surface static voltage of approximately −0.34 kV. Furthermore, the composite scaffold can continuously output voltage under sustained mechanical force stimulation. Both cell experiments and animal studies demonstrated that this scaffold can effectively modulate immunity and facilitate osteogenesis. This research presents an innovative approach to developing in-situ self-powered 3D-printed scaffolds that achieve self-power by integrating the shape memory process and piezoelectric effects, providing a simple and efficient method for in-situ electrical stimulation in bone defect repair.

Materials and methods

Materials

Polyvinylidene Fluoride (PVDF) was purchased from Macklin. Polycaprolactone diol (PCL) with a molecular weight (Mn) of 2000 was purchased from Aladdin. Hexamethylene diisocyanate (HDI) and castor oil were also purchased from Aladdin. *N*, *N*-dimethylformamide (DMF), and hexafluoroisopropanol were obtained from Innochem; acetone was purchased from Sinopharm. All reagents were used as received without any pretreatment.

Fabrication of arranged and random PVDF nanofibers

Two types of PVDF nanofibers were prepared using electrospinning technology (SS-3556H, Yongkang Leye Technology Development, China). The PVDF particles were mixed with a solvent mixture of DMF and acetone (mass ratio: 2:3), and the solution was stirred overnight at 80 ℃. After cooling to room temperature (23 ± 2 ℃), nanofibers were fabricated via electrospinning technology. The electrospinning parameters were set as follows: a solution feed rate of 1 mL/h, a high voltage of 20 kV, a distance of 13 cm between the needle and collector, and a collector rotation rate of 2000 rpm.

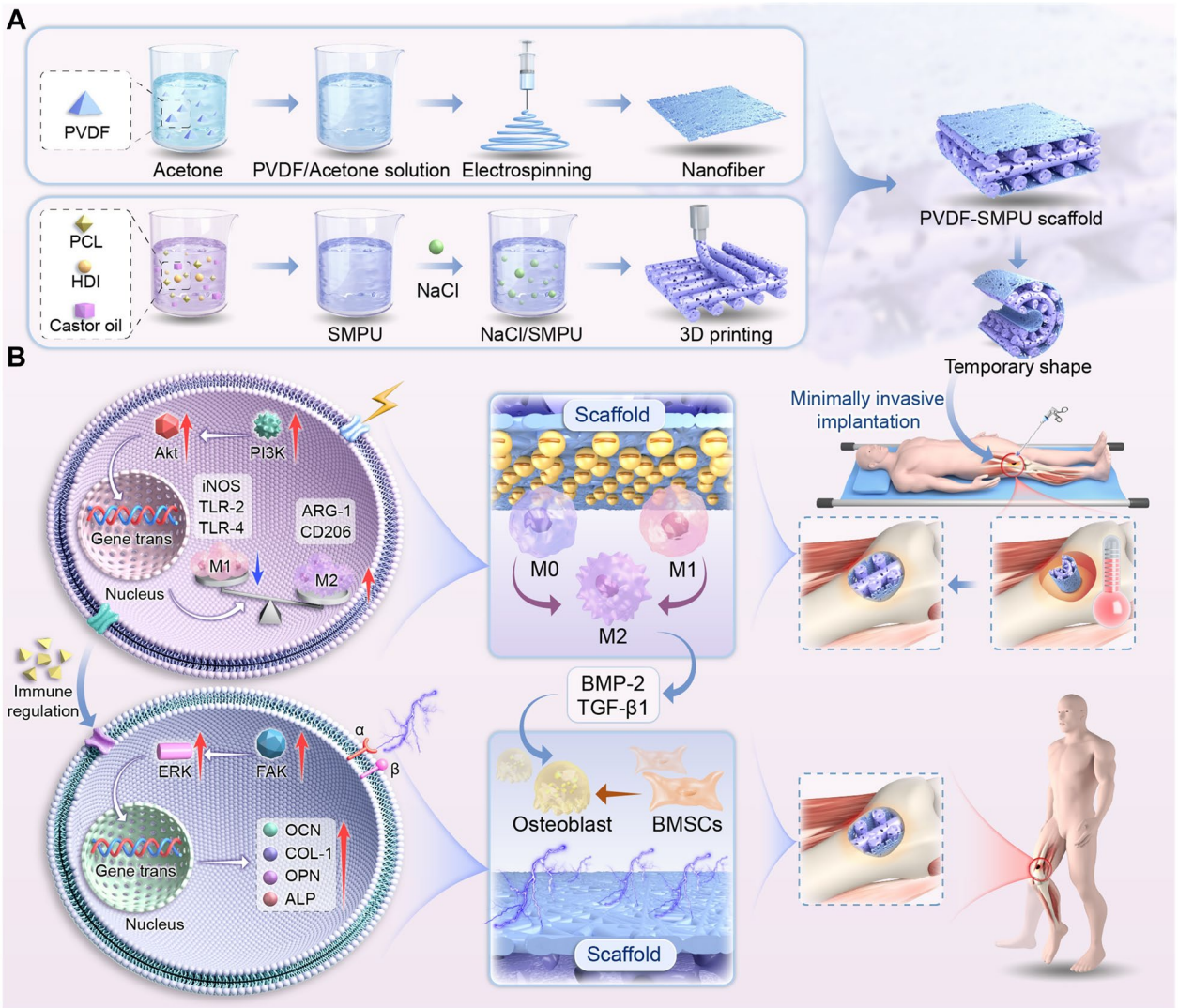

Fig. 1 Schematic diagram of preparation and design concept of the 3D printed in-situ self-powered scaffold. **A** The preparation process of the 3D printed in-situ self-powered scaffold. **B** The mechanism of achieving in-situ self-power in vivo by integrating the shape memory process and piezoelectric effect. The scaffolds feature a customized structure capable of structural and functional transformation triggered by physiological temperature, which can be used for minimally invasive implantation. During the initial postoperative period, the scaffold can generate electrical charge through the shape memory process to modulate the immune microenvironment. As treatment progresses, continuous mechanical force stimulation can be applied to the scaffold through rehabilitation exercises when the patient regains exercise ability, enabling the scaffold to output voltage and stimulate stem cell osteogenic differentiation

Characterization of PVDF nanofibers

The microstructure of PVDF nanofibers was analyzed using a scanning electron microscope (SEM, JSM-7500F, JEOL Japan), and the scanning voltage was set at 15 kV. X-ray diffraction (XRD, Bruker D8 ADVANCE, Germany) and Fourier-transformed infrared spectroscopy (FT-IR, NICOLET iS10, USA.) were employed to analyze the crystalline structure of the nanofibers.

Fabrication of SMPU printable ink and scaffolds

In order to make SMPU have high repeatability, the material formulation and experimental conditions have been optimized several times, and finally, a mature preparation process has been obtained. All samples were prepared in the same time frame, using the same equipment and conditions, further enhancing the sample's repeatability. SMPU prepolymers were prepared as follows. First, PCL and castor oil were dehydrated at 80 ℃ under vacuum conditions for 12 h. Then, PCL, castor oil, and HDI were mixed and stirred at 90 ℃ under a nitrogen

atmosphere for 40 min to synthesize polyurethane prepolymer. The resulting polyurethane prepolymer was mixed with sodium chloride (NaCl) particles (mass ratio: 1:2.5) to prepare the printable ink. The SMPU scaffold was fabricated using fused deposition modeling (FDM) technology (Bio-Architect®SR, Regenovo, China). The processing parameters were as follows: a scanning rate of 0.001 mm/s, a needle diameter of 500 μm, and material barrel and needle temperature of 60 ℃ and 50 ℃, respectively. After printing, the scaffold was cured at 80 ℃ for 24 h. Subsequently, it was soaked in ultrapure water to eliminate the NaCl particles.

Fabrication of PVDF-SMPU composite scaffolds

The composite scaffolds were prepared by adhering PVDF nanofibers to the SMPU scaffolds. First, an adhesive solution was prepared by dissolving PCL (molecular weight: 50,000) in hexafluoroisopropanol at a mass ratio of 15%. The SMPU scaffold surface was coated with PCL solution as an adhesive layer. The PVDF nanofiber was then attached to the scaffold surface to form a composite scaffold. The composite scaffold was subsequently dried in an oven (40 ℃, 48 h) to eliminate residual hexafluoroisopropanol.

Microstructural analysis of SMPU scaffolds and PVDF-SMPU composite scaffolds

FT-IR was conducted to confirm the successful synthesis of SMPU, and the spectral wavelength range was recorded as 4000–400 cm^{-1}. The microstructure of SMPU scaffold and PVDF-SMPU composite scaffold was observed using an SEM.

In vitro shape memory performance analysis of SMPU scaffolds and PVDF-SMPU composite scaffolds

The scaffold's shape transition temperature was evaluated using differential scanning calorimetry (DSC, DSC2500, TA USA). The scaffold's shape memory performance was evaluated by dynamic mechanical analysis (DMA, DMA850, TA USA).

In vivo shape memory performance analysis of SMPU scaffolds

To evaluate the in vivo minimally invasive implantation and shape memory process of the composite scaffold, a male Sprague Dawley rat weighing 170 g and aged three weeks was anesthetized using pentobarbital sodium, and the indocyanine green-loaded temporary shape memory scaffold was implanted subcutaneously using a minimally invasive procedure. The shape memory behavior of the scaffold under physiological temperature was monitored using an imaging system (IVIS®Lumina III, PerkinElmer, USA).

Degradation behavior and surface hydrophilicity analysis of SMPU scaffolds and PVDF-SMPU composite scaffolds

A contact angle detector (DSA30, Germany) was used to measure the scaffold's water contact angle (WCA). Degradation assays were performed in triplicate by incubating preweighed scaffolds ($1\times1\times1$ cm^3) in 10 mL of PBS solutions containing 2000 U/mL lipase (pH = 7.4) at 37 ℃ under agitation (60 rpm) for 7 days. At the end of each time point, the scaffolds were carefully extracted, rinsed with water, dried, and weighed to quantify degradation.

Piezoelectric properties of PVDF nanofibers and PVDF-SMPU composite scaffolds

A quasi-static d_{33} piezoelectric coefficient testing device (ZJ-3A, China) was used to measure the piezoelectric coefficient (d_{33}) of PVDF nanofibers. All samples (2.5×2.5) used for d_{33} testing were prepared under the same conditions, and three groups of parallel samples at the same annealing temperature underwent the same annealing process. Before testing, all samples underwent the same polarization process with an oil bath polarization mode and a 3 kV polarization electric field. To investigate the changes in the surface static voltage under ultrasound and mechanical force stimulation, a surface static voltage detector (JH-TEST, China) was used to measure the surface static voltage of the nanofibers (3×3 cm) at varying ultrasound power (0 W/cm^2, 0.4 W/cm^2, 0.5 W/cm^2 and 0.6 W/cm^2) and different levels of mechanical force intensities (0 N, 1 N, 2 N, 3 N, 4 N and 5 N; tensile force). The voltage output of the composite scaffold under continuous mechanical force stimulation was measured using an ultrasonic therapy device (DJO 2776, USA) and a mechanical impact device, and the output voltage was recorded through an electrometer (Keithley 6514, USA). The sample preparation process was as follows: the top and bottom of a composite scaffold (3×3 cm) were connected with two copper foils as the upper and lower electrodes, respectively, to form a sandwich-like structure, and the upper and lower electrodes were in close contact with the sample. The copper foil size was 2×2 cm to prevent short circuits from contacting the upper and lower electrodes. Then, copper wires were connected to the bottom and top electrodes for wiring. Note that the wiring directions of the two copper wires need to be staggered to prevent short circuits from contact. Two PET sheets (5×5 cm) were placed on the electrode with tape, and pressure was applied to make the sample compact and avoid triboelectric effects. To detect voltage output under ultrasound stimulation, the prepared sample was placed in close contact with the probe of the ultrasound therapeutic device, and two copper wires were connected to the electrometer. The ultrasound frequency was set to 1 MHz, and the output

power of the ultrasound therapeutic device was adjusted (1 W/cm^2, 1.5 W/cm^2, and 2 W/cm^2) to detect the voltage output of the sample at different ultrasound powers. For the voltage output under repeated mechanical impact conditions, the sample was fixed to the force plate of the mechanical impact device, and two copper wires were connected to the electrometer. The distance between the mechanical lever arm and the sample was adjusted so that each mechanical impact produced a compressive strain of 2% on the sample. The impact frequency was set as two cycles per second. A surface static voltage detector was used to monitor the surface electrostatic potential before and after the shape memory process.

Methods for biomineralization, in vitro biocompatibility, immunofluorescence staining, RT-qPCR, Western blot, and in vivo bone defect repair performance evaluation, etc. were described in the Experimental Section of supplementary materials.

Statistical analysis

Quantitative data were analyzed using one-way analysis of variance (ANOVA) using Origin 8.5. Results were presented as the mean ± standard deviation for $n \geq 3$. A p-value ≤ 0.05 is considered statistically significant, while a p-value ≤ 0.01 indicates a highly significant difference between groups.

Results and discussion

Preparation and characterization of PVDF nanofibers

As a piezoelectric polymer, PVDF has excellent biocompatibility and remarkable piezoelectric properties and can generate polarized charges similar to naturally piezoelectric bone tissue when subjected to mechanical force stimulation. Additionally, PVDF can deform under mechanical force stimulation due to its good flexibility, allowing it to adapt to the shape change of the composite scaffold. Therefore, we chose PVDF as the piezoelectric component for the composite scaffold. Two types of PVDF nanofibers were prepared using the electrospinning technology (Fig. 2A). The PVDF nanofibers with aligned fibers were named A-PVDF, while the others with random fibers were named R-PVDF. SEM images (Fig. 2B) revealed that A-PVDF exhibits a highly aligned fiber orientation, whereas R-PVDF shows a random fiber orientation. The average fiber diameters were measured as 430 ± 7 nm (A-PVDF) and 470 ± 5 nm (R-PVDF). The crystalline phase of PVDF is essential for its piezoelectric characteristics, and the β phase is recognized for exhibiting the most significant piezoelectric activity among the five crystalline forms in PVDF [31–36]. Additionally, annealing can enhance the β-phase content of PVDF significantly [34]. In this study, PVDF nanofibers were subjected to annealing to increase the β phase content. XRD and FT-IR analyses (Fig. 2C, D) confirmed that the original A-PVDF exhibited a higher β phase content than the original R-PVDF. Under identical annealing conditions, the A-PVDF also had higher β phase content than R-PVDF. This result is attributed to the stronger mechanical stretching experienced by A-PVDF during the preparation process, which increases its polarization degree, resulting in a higher β phase content. The above findings indicate that the A-PVDF has a higher β phase content than R-PVDF and exhibited the highest β phase content after being annealed at 120 ℃.

The piezoelectric coefficient d_{33}, a vital parameter in describing piezoelectric performance, represents the proportional relationship between the charge generated by the piezoelectric strain along a particular direction and the applied electric field under the action of the electric field. The d_{33} values of PVDF nanofibers were measured to evaluate their piezoelectric properties (Fig. 2E). The results showed that the d_{33} values for the original A-PVDF (4.3 ± 0.2) were higher than those of the original R-PVDF (4.0 ± 0.1). After annealing at 120 ℃, the d_{33} values increased to 7.9 ± 0.1 for A-PVDF and 6.2 ± 0.3 for R-PVDF. This result indicates that annealing at 120 ℃ leads to the highest d_{33} values. The annealing process can promote the transformation of the non-polar α-phase into the polar β-phase. During the annealing process, the internal stresses within the PVDF are relieved, allowing the polymer chains to reorganize under thermodynamic driving forces. This reorganization promotes the transformation of the non-polar α-phase into the polar β-phase, which is known for its superior piezoelectric properties [37–39]. Based on these findings, all the nanofibers used in the subsequent experiments were annealed at 120 ℃. According to the literature, PVDF can generate charge under mechanical force stimulation, and the charge can accumulate on the surface, forming static voltage [40]. Ultrasound stimulation and tensile force were applied to PVDF nanofibers to evaluate their piezoelectric performance further. As shown in Figure S1, increasing ultrasound power and tensile force resulted in higher surface static voltage for both A-PVDF and R-PVDF. However, A-PVDF consistently displayed a higher surface static voltage under identical conditions, highlighting its superior piezoelectric performance.

Previous studies have demonstrated that the PVDF can output voltage when subjected to repeated bending deformation under continuous mechanical force stimulation, and higher mechanical force stimulation can cause larger bending angles, resulting in higher voltage output [41]. Therefore, to evaluate the voltage output performance of PVDF nanofibers under continuous mechanical force stimulation, the voltage output of PVDF nanofibers was measured by repeatedly bending the PVDF

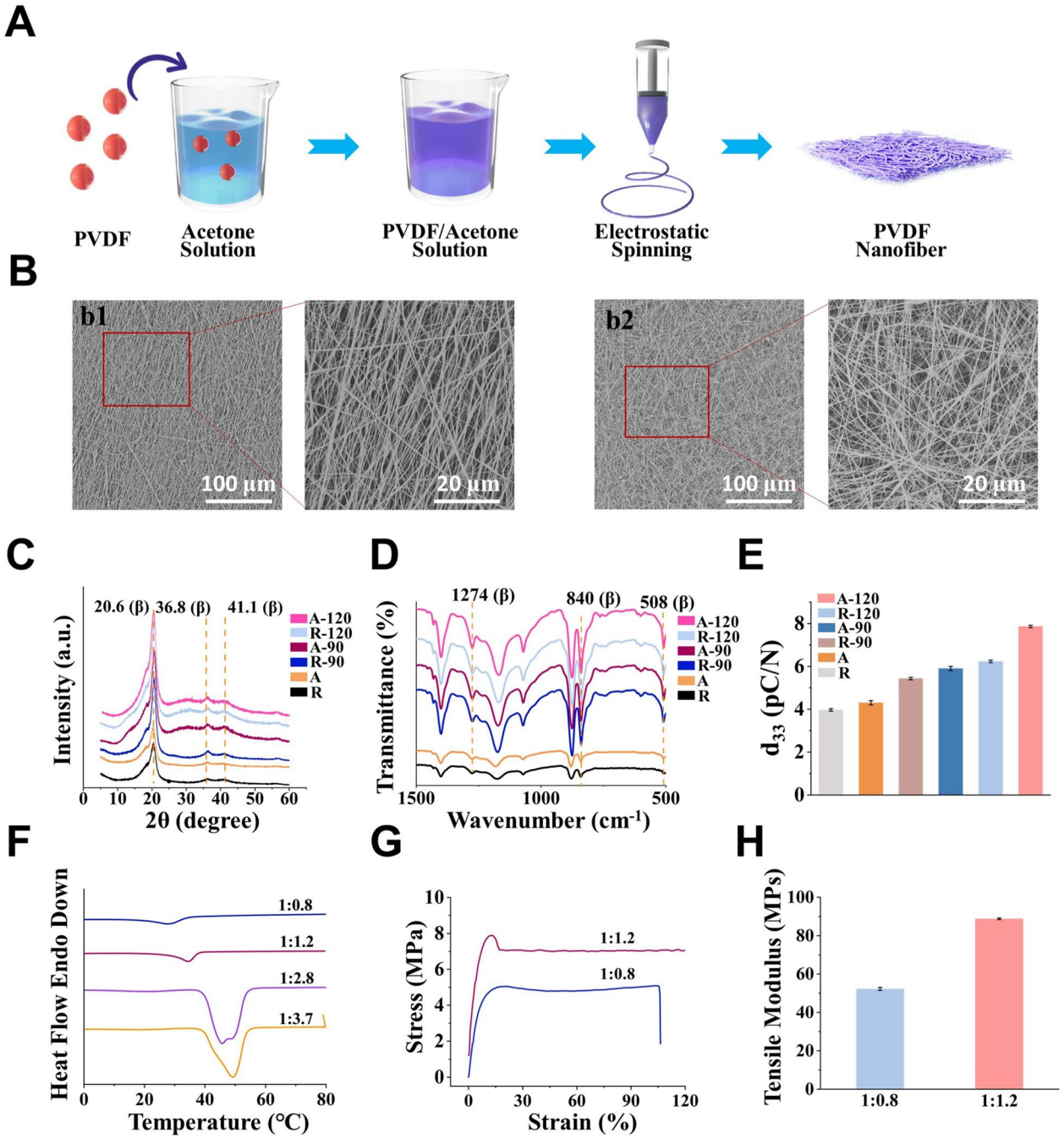

Fig. 2 Characterization of PVDF nanofibers. **A** The preparation process of PVDF nanofibers; **B** The SEM image of PVDF nanofibers (b1: aligned fibers; b2: random fibers). **C**, **D** The FT-IR and XRD pattern of PVDF nanofibers after annealing treatment at different annealing temperatures (A: aligned fibers (A-PVDF); R: random fibers (R-PVDF); **E** The piezoelectric coefficient of PVDF nanofibers after annealing treatment at different annealing temperatures; **F** The DSC curves of SMPU with different PCL: castor oil molar ratios; **G**, **H** The stress–strain curves of SMPU and corresponding tensile modulus (n = 3; error bars represent standard deviation)

nanofibers at various angles (Figure S2). Results showed that both nanofibers could continuously output voltage, with the voltage output increasing proportionally to the bending angle. Additionally, A-PVDF exhibited superior voltage output compared to R-PVDF. These results confirm that the prepared PVDF nanofibers possess excellent piezoelectric properties and can generate charge under mechanical force stimulation.

Preparation and characterization of SMPU

The shape memory component is another critical component in the composite scaffold besides piezoelectric materials. The PVDF can experience deformations such as bending and stretching when the composite scaffold undergoes shape changes such as compression, bending, and stretching. Consequently, the composite scaffold can apply mechanical force stimulation to the PVDF to generate charge through the scaffold's shape memory process, achieving in-situ self-power. Additionally, the shape memory properties contribute to the composite scaffold's minimally invasive implantation capability. The composite scaffold can be compressed to a minimal size before implantation, allowing it to pass through smaller incisions and recover the original size under physiological temperature. In this study, SMPU was selected as the shape memory component due to its exceptional shape memory performance, biocompatibility, and ease of fabrication. The SMPU prepolymer was synthesized using a one-step method using PCL, HDI, and castor oil as raw materials (Figure S3). In this formulation, PCL is the soft segment, providing flexibility and toughness. HDI is the hard segment, offering hardness and wear resistance. Castor oil plays a role in plasticization and toughening. The FT-IR analysis of the synthesized SMPU is shown in Figure S4. The peaks observed at 3390 cm^{-1} and 1722 cm^{-1} are attributed to the stretching vibrations of –N–H and C=O groups, respectively, which suggests the presence of an amide bond. The characteristic peak (2250 ~ 2270 cm^{-1}) for the NCO– group is not found in the spectrum, indicating that the NCO- group reacts completely [42, 43]. The above results validate the successful preparation of SMPU.

The melting temperature (Tm) is a critical parameter of temperature-response SMPs representing the threshold that triggers the shape memory behavior. In this study, SMPUs with varying molar ratios of PCL to castor oil were prepared, and their Tm values were determined using DSC (Fig. 2F). Results showed that decreasing the molar ratio of PCL led to an increase in Tm. The reduction of PCL content is accompanied by the increase of castor oil content, which increases the length of the molecular chain in SMPU and improves its heat resistance [42, 44, 45]. Because the shape recovery of the scaffold needs to be triggered by physiological temperatures, the Tm of the SMPU must be below 37 ℃. In the above samples, the Tm of SMPUs with a molar ratio of PCL to castor oil of 1:0.8 and 1:1.2 is below 37 ℃. To obtain the SMPU with optimal mechanical properties in which the Tm is below 37 ℃, tensile testing was performed on the two SMPUs (Fig. 2G). Analysis of the stress–strain curves revealed tensile moduli of 53 ± 1.7 MPa for SMPU (1:0.8) and 88 ± 1.2 MPa for SMPU (1:1.2) (Fig. 2H). The results indicated that increasing castor oil content enhanced the mechanical properties of SMPU. Furthermore, evaluation of maximum tensile strain (Figure S5) showed that SMPU (1:1.2) achieved a maximum tensile strain of 1164%, compared to 769% for SMPU (1:0.8). This result highlights that SMPU (1:1.2) exhibits superior tensile performance and ductility, enabling it to undergo more considerable shape change during the shape memory process.

The shape memory process of SMPs involves energy absorption and release [46, 47]. The work output is a key indicator of energy release performance and reflects the amount of mechanical energy released during the shape recovery process [48]. A higher work output indicates that the SMPs can release more mechanical energy during the shape recovery process. In this study, to assess the work output of the SMPU, pre-stretched SMPU thin splines were subjected to a 100 g load, and shape recovery was triggered using a heat source. Results (Figure S6) showed that SMPU (1:1.2) exhibited significantly higher work output compared to SMPU (1:0.8). This finding suggests that increasing the castor oil content enhances the energy release capability of SMPU during shape recovery, enabling the scaffold to apply greater mechanical force stimulation to the PVDF and generate more charge.

Based on the above results, the SMPU (1:1.2) was selected for subsequent scaffold preparation. This formulation combines excellent mechanical properties, high ductility, and superior work output while maintaining a Tm of 33 ℃, which can trigger shape recovery under physiological conditions.

To evaluate the degradation behavior of SMPU, SMPU samples were immersed in PBS containing 2000 U/mL lipase at 37 ℃. The degradation kinetics of SMPU (Figure S7) showed that the degradation rate of SMPU can reach 9.8% within 7 days, demonstrating its favorable degradation characteristics and is suitable for bone defect repair.

Preparation and characterization of PVDF-SMPU composite scaffold

The SMPU prepolymer was mixed with NaCl particles (60–80 μm) in a series of proportions (1:1, 1:2.5, and 1:3 for mass ratio) to prepare the printable ink. To determine the appropriate proportion of ink composition, the ink cylinders were fabricated for shape retention experiments. Considering the curing temperature of polyurethane, which ranges from 60 ℃ to 80 ℃ [49], the shape retention experiments were conducted at 80 ℃. The results (Figure S8) indicated that the ink cylinders achieved optimal shape retention when the mass ratio of SMPU to NaCl was equal to or exceeded 1:2.5. Additionally, although the shape retention performance of the printable ink with a mass ratio of 1:3 was better than that of the printable ink with a mass ratio of 1:2.5, we found

that the printable ink with this mass ratio was difficult to print smoothly in the subsequent printing process of the scaffold, which was manifested as difficult extrusion and the extruded filament was easy to break. Consequently, the mass ratio of 1:2.5 was selected for the subsequent scaffold printing. The SMPU scaffold was fabricated using FDM technology (Fig. 3A). Figure S9 presents the overall image and SEM image of the SMPU scaffold before and after the removal of NaCl particles. The result demonstrated that the scaffold maintained its structural integrity after removing NaCl particles and exhibited porous microstructure. Figure 3B illustrates the scaffold's morphology at both macroscopic and microscopic levels. The prepared scaffold had a three-dimensional porous structure, which could fill defect sites and promote cell proliferation and migration in bone repair. The mechanical properties analysis of the SMPU scaffold (Fig. 3C) revealed a compressive modulus of 2.4 ± 0.4 MPa. These results indicate that the scaffold possesses a three-dimensional porous structure with favorable mechanical properties, making it suitable for bone tissue engineering.

DMA was used to assess the scaffold's shape memory capabilities (Fig. 3D), and the result showed that the scaffold could maintain a fixed shape well. Upon heating, the scaffold could gradually recover to its original shape. The shape fixity rate (Sf) and shape recovery rate (Sr) of the scaffold exceed 98% (Figure S10), indicating excellent shape memory performance. As the temperature exceeds Tm, the soft segments within the SMPU molecular chain transition from a crystalline state to a molten

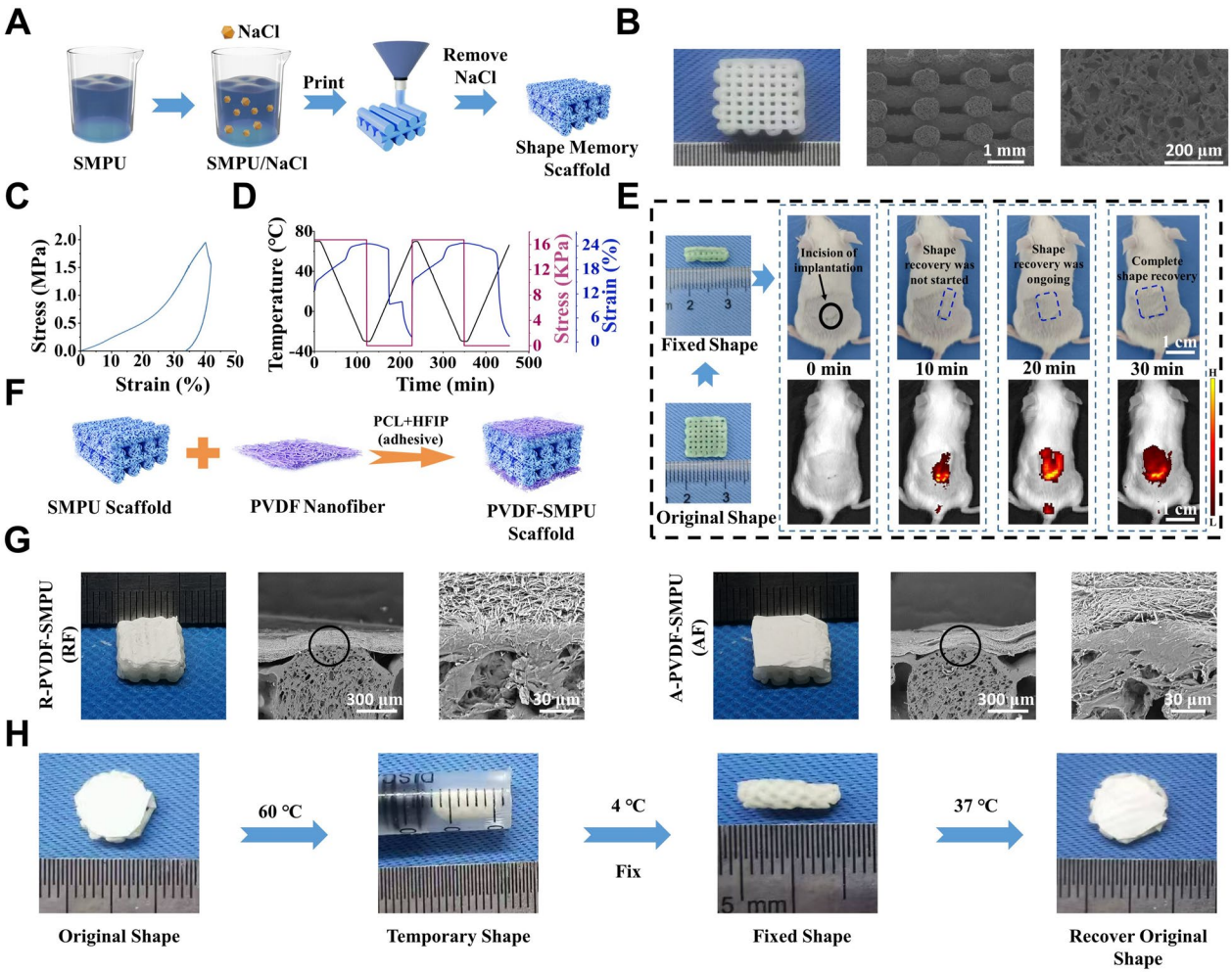

Fig. 3 The shape memory properties of scaffolds. **A** The preparation process of the SMPU scaffold; **B** The overall image and SEM image of the SMPU scaffold; **C** The stress–strain curve of the SMPU scaffold, the strain range used for measurement is 0%–10%; **D** The DMA curve of the SMPU scaffold; **E** In vivo simulation of the SMPU scaffold for the minimally invasive implantation and shape memory process; **F** The preparation process of the PVDF-SMPU composite scaffold; **G** The overall image of the composite scaffold and the SEM image of the bonding interface of PVDF and SMPU in the composite scaffold; **H** In vitro simulation of composite scaffolds (AF) for the shape memory process. n = 3

state, then the SMPU can deform and be prepared into various shapes under external forces. As the temperature drops below Tm, the soft segments will crystallize again, allowing the SMPU to retain a fixed temporary shape. Once the temperature rises above the Tm again, the molecular chains can transition from a crystalline state to a molten state again, and the presence of hard segments can prevent plastic deformation during the deformation process, contributing to an enhanced ability of the SMPU to recover its original shape. To evaluate the minimally invasive implantation capability of the scaffold, a compressed scaffold was implanted into a simulated bone defect model and underwent a shape recovery at 37 ℃. The results (Figure S11) showed that the scaffold fully recovered its original shape and filled the defect site under physiological temperature conditions (37 ℃), demonstrating that the scaffold exhibits excellent shape memory performance and can fulfill the requirements for minimally invasive implantation.

To further assess the scaffold's minimally invasive implantation performance and physiological temperature-triggered shape recovery performance, a scaffold loaded with the fluorescent dye indocyanine green was fixed in a temporary shape and implanted subcutaneously in rats via a minimally invasive approach. Fluorescence imaging was employed to monitor the scaffold's shape recovery at physiological temperature. As shown in Fig. 3E, the compressed scaffold was implanted through a small incision and fully recovered its original shape within 30 min at physiological temperature, confirming excellent shape memory performance and minimally invasive implantation performance.

PVDF nanofibers were bonded onto the SMPU scaffold's surface with a PCL adhesive to prepare the composite scaffold (Fig. 3F), the composite scaffold was denoted as PVDF-SMPU, and this design combines the shape memory properties of SMPU with the piezoelectric properties of PVDF to create a multifunctional scaffold for bone defect repair. Figure 3G displayed the morphological characteristics of the composite scaffold at both macroscopic and microscopic levels. The SEM images reveal an intense and fused interface between the nanofibers and the SMPU scaffold, which ensures tight bonding between the scaffold and nanofibers. This robust interface prevents PVDF detachment or loosening during the shape change process of the composite scaffold, enabling the PVDF to adapt fully to the composite scaffold's shape memory behavior and receive mechanical force stimulation. Figure 3H illustrates the shape memory capabilities of the composite scaffold. The composite scaffold was deformed into a temporary shape at 60 ℃, fixed at 4 ℃, and returned to its original shape once heated to 37 ℃. These results further demonstrated the shape memory performance of the composite scaffold. Notably, the PVDF nanofibers can undergo deformation during the composite scaffold's shape memory process and remain tightly bonded post-recovery, further validating the interface's stability. This strong adhesion ensures that the PVDF nanofibers fully receive mechanical force stimulation from the composite scaffold during the shape memory process, thereby achieving optimal piezoelectric effects.

In vitro biocompatibility evaluation of PVDF-SMPU composite scaffold

Biocompatibility is a critical challenge for the tissue engineering application of piezoelectric electronic devices. In this study, to evaluate the biocompatibility of the composite scaffold, CCK-8 assays and live/dead fluorescent staining were performed. Prior to biocompatibility evaluation, the WCA was measured to evaluate the composite scaffold's surface hydrophilicity. As shown in Figure S12, the WCA of A-PVDF-SMPU (AF) was 64 ± 1.7°, and the WCA of R-PVDF-SMPU (RF) was 60 ± 2.3°. It is known that a water contact angle between 60° and 80° is generally considered to be the optimal range for cell adhesion and proliferation. Specifically, a contact angle of about 80° can effectively promote the adhesion and proliferation of bone marrow mesenchymal stem cells (BMSCs) [50, 51]. Additionally, it has been shown that a water contact angle of about 60° is also beneficial for the adhesion and proliferation of macrophages and BMSCs [52]. This result indicates that both scaffolds have good hydrophilicity, which is beneficial for the adhesion and proliferation of BMSCs and macrophages and can be used in subsequent cell and animal experiments.

Bone marrow mesenchymal stem cells (BMSCs) were used to assess the biocompatibility of the composite scaffold. The CCK-8 results are shown in Fig. 4A. The results demonstrated that all composite scaffolds exhibited

(See figure on next page.)

Fig. 4 In vitro biocompatibility assessment. **A** The CCK-8 result of BMSCs treated with different scaffolds. **B** SEM images of BMSCs seed on the scaffold surface after 24 h **C** Live/dead fluorescent staining result of BMSCs treated with different scaffolds (red fluorescence indicates dead cells, green fluorescence indicates live cells). **D** Immunofluorescence staining result of BMSCs treated with different scaffolds (blue represents cell nuclei, red represents actin network). The control group was operated without scaffold treatment. **$p < 0.01$, highly significant ($n = 3$; error bars represent standard deviation)

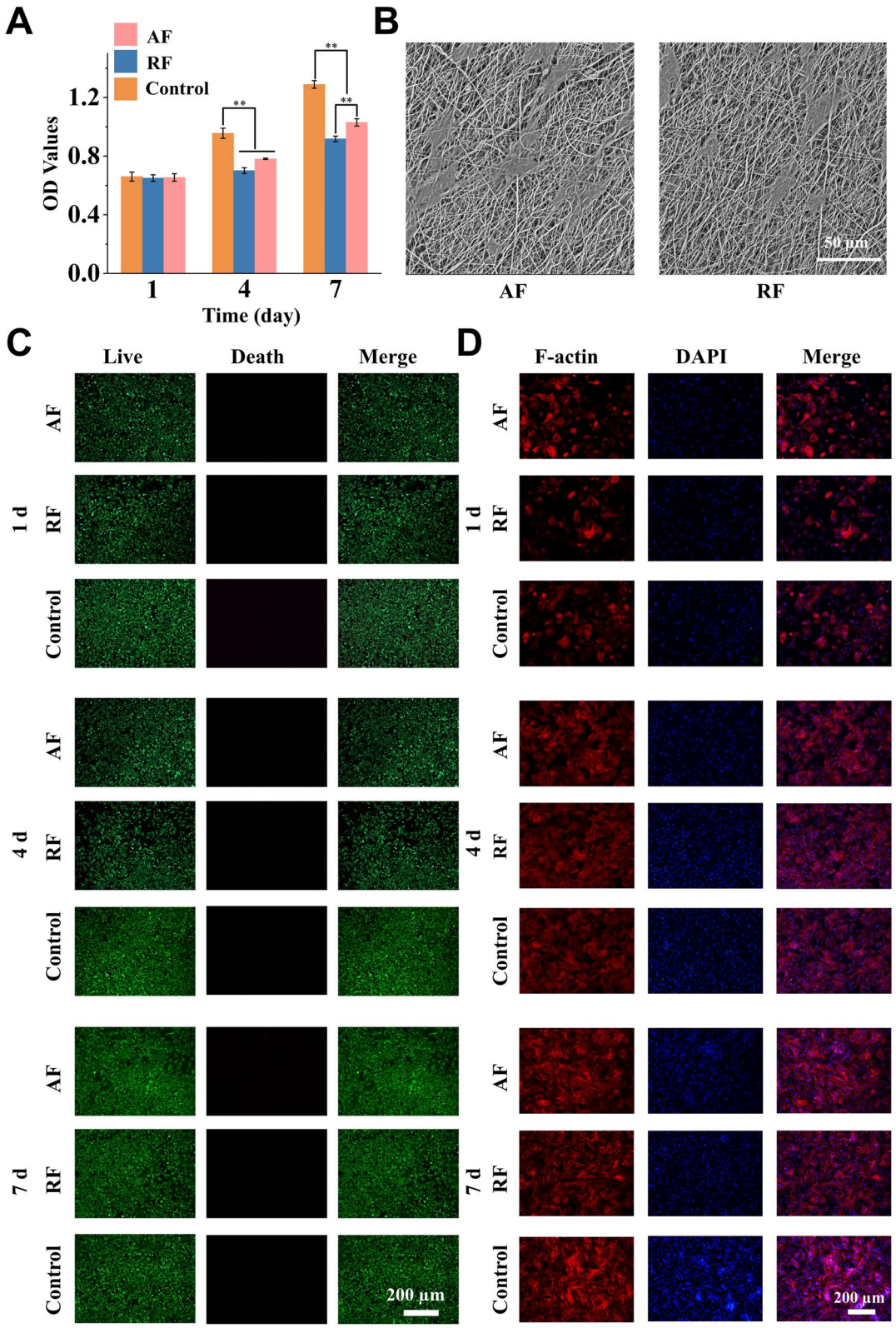

Fig. 4 (See legend on previous page.)

excellent cell compatibility, with the cells treated with the composite scaffold continuously proliferating. The SEM was performed to observe the cell morphology on the composite scaffold surface (Fig. 4B). The results showed that BMSCs exhibited normal adhesion on the scaffold surface, displaying no abnormal morphology. Filopodia-like extensions of the cells were observed, demonstrating the composite scaffold's favorable biocompatibility. Live/dead fluorescence staining was conducted to evaluate the composite scaffold's biocompatibility (Fig. 4C). The results showed that BMSCs in all experimental groups survived and proliferated normally, further demonstrating the biocompatibility of the composite scaffold. Additionally, because the BMSCs could adhere and proliferate normally in each experimental group, and the number of cells in each experimental group was sufficient, the visual difference between the staining results of the experimental groups was minor. The quantitative analysis results of live/dead fluorescence staining also showed that the composite scaffold had good biocompatibility and could continuously promote cell proliferation (Figure S13A and S13B). The hemolysis test further proved the biocompatibility of the scaffold. According to the results (Figure S14), the hemolysis rates of all the scaffolds were lower than 0.4, while complete hemolysis occurred in the positive control group (H_2O), which proved the excellent biocompatibility of the scaffold. The cell scratch results (Figure S15) indicated that the AF group exhibited the most excellent cell migration effect, indicating that the composite scaffold can effectively promote cell migration and diffusion. Immunofluorescent staining of the cytoskeleton and nuclei (Fig. 4D) revealed that BMSCs cultured with the composite scaffolds exhibited typical stem cell morphology, with well-organized actin networks and intact nuclei, confirming the favorable biocompatibility of the composite scaffold. Similar to the results of live/dead fluorescence staining, because all experimental groups had good biocompatibility and the number of BMSCs was sufficient, the visual difference between the staining results of the experimental groups was minor. The quantitative analysis results of immunofluorescence staining (Figure S13C) also showed that the composite scaffold had good biocompatibility and could continuously promote cell proliferation. The above findings confirm that the composite scaffold does not adversely affect the morphology, adhesion, or proliferation of BMSCs. In conclusion, the composite scaffold exhibited excellent biocompatibility and holds great potential for subsequent immunological and osteogenic analyses.

In vitro macrophage phenotype modulatory performance evaluation of PVDF-SMPU composite scaffold

Patients with bone defects often experience limited mobility during the initial postoperative stage, which restricts their ability to provide mechanical force stimulation to scaffolds through rehabilitation exercises. Previous shape memory characterization demonstrated that the composite scaffold possesses excellent shape memory performance, enabling recovery to its original shape at physiological temperatures. During this shape recovery process, the composite scaffold can output mechanical energy, which can stimulate PVDF to produce charge (Fig. 5A, B). To evaluate the charge generation capability of the composite scaffold during the shape memory process, the surface static voltage of the composite scaffold was measured using a surface static voltage detector before and after the shape recovery. The scaffold was then immersed in PBS, and its surface static voltage was remeasured after 7 days to evaluate its stability (Fig. 5C). The results show that the surface static voltage significantly increased after the shape memory process, and the AF exhibited the highest surface static voltage of −0.34 kV, indicating that the composite scaffold can provide mechanical force stimulation to PVDF to generate charge through the shape memory process. Furthermore, after immersion in PBS for 7 days, the surface static voltage remained above −0.14 kV. Since PBS contains a large number of ions, such as calcium ions and phosphate ions, the surface charge of the composite scaffold will bind to these ions, causing a decrease in the surface static voltage. After the process reaches equilibrium, the decreasing speed of the surface static voltage of the composite scaffold will be greatly slowed down and maintained in a relatively stable state [53–56]. According to the literature, the surface static voltage in the range of −0.1 kV to

(See figure on next page.)

Fig. 5 In vitro evaluation of macrophage phenotype modulation. **A** Schematic representation of the charge generated and accumulated on the composite scaffold after undergoing the shape memory process; **B** Original composite scaffold culture with cells; **C** Surface static voltage of the composite scaffold before and after the shape memory process and after 7 days in PBS (SP: the composite scaffold undergoes shape memory process); **D** The expression of phenotype-related genes ARG-1 (M2), CD206 (M2), iNOS (M1), TLR-2 (M1), and TLR-4 (M1) in RAW264.7 cells treated with different composite scaffolds; **E** Immunofluorescence staining results of CD86 (M1) and CD206 (M2) expression in RAW264.7 cells treated with different composite scaffolds. **F** Analyzed macrophage polarization by flow cytometry in RAW264.7 cells treated with different composite scaffolds. The control group was operated without scaffold treatment. *$p < 0.05$, significant **$p < 0.01$, highly significant ($n = 3$; error bars represent standard deviation)

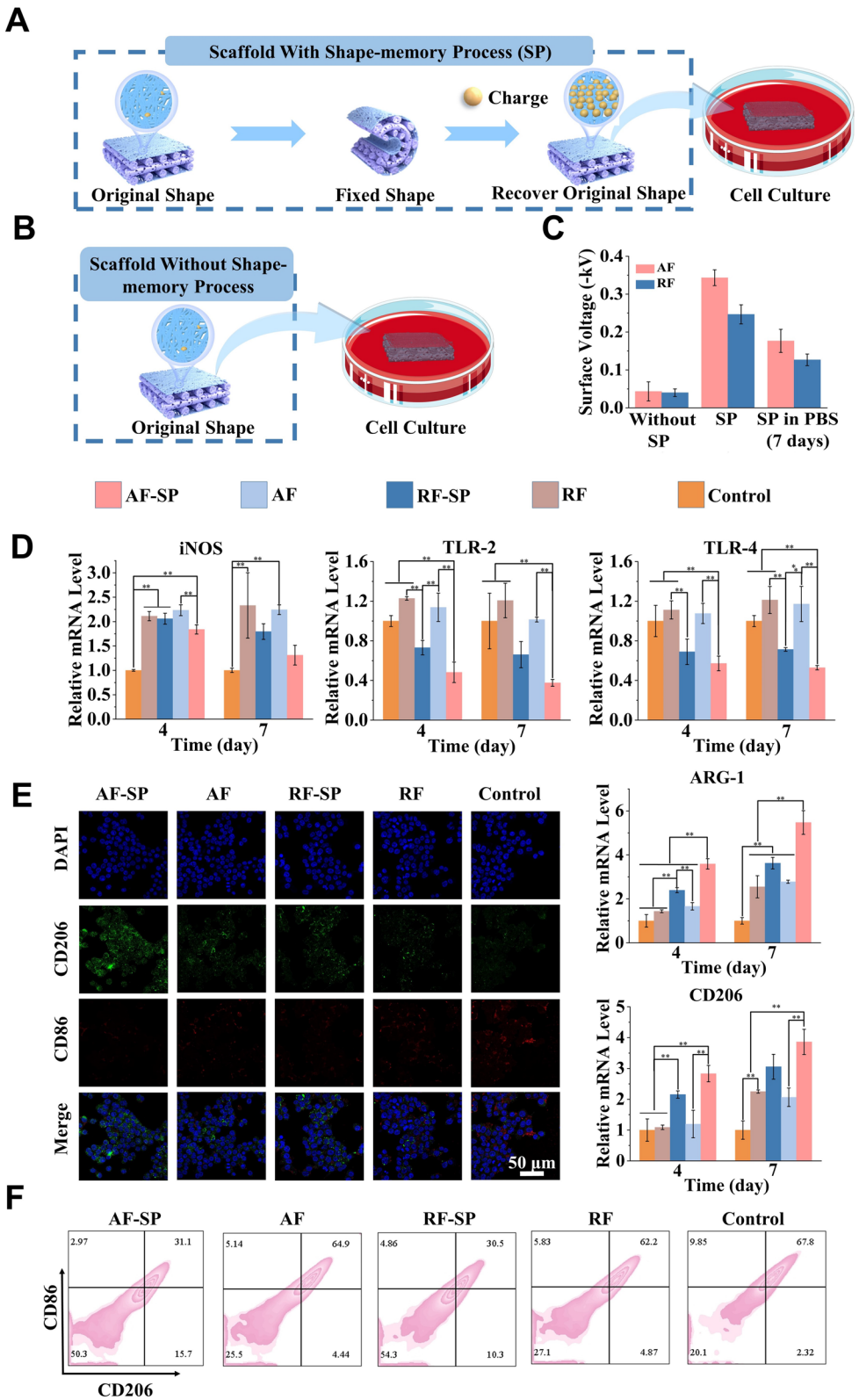

Fig. 5 (See legend on previous page.)

−4.9 kV contributed to bone defect repair. In particular, the surface static voltage from −0.1 kV to −0.25 kV showed good immunoregulatory and osteogenic effects, indicating that the composite scaffold could meet the requirements of immunoregulation and osteogenesis [53, 57]. These findings indicate that the composite scaffold integrates the shape memory process with a piezoelectric effect, enabling in-situ electrical stimulation in the form of self-power for bone defect patients with limited exercise ability during the initial postoperative period.

The regulation of the immune microenvironment during the initial stages of scaffold implantation is critical for achieving successful bone repair [2, 58]. Previous studies have confirmed the important role of macrophages in immune regulation [59]. Electrical stimulation can induce macrophages to polarize from the M1 to the M2 phenotype, with M2 macrophages capable of releasing factors that regulate the inflammatory response and promote stem cell osteogenic differentiation [2, 60]. RAW264.7 cells were used to assess the immunomodulatory performance of the composite scaffold (Fig. 5A, B). Composite scaffolds that underwent the shape memory process were designated AF-SP and RF-SP, while those that did not were named AF and RF. The gene expression levels of macrophage phenotypic markers were analyzed using RT-qPCR (Fig. 5D). Macrophages treated with AF-SP exhibited the highest gene expression levels associated with the M2 phenotype and the lowest expression levels related to the M1 phenotype. These findings confirm that the composite scaffold can provide mechanical force stimulation to PVDF to generate charge through the shape memory process, and the charge can promote macrophage M2 polarization. During the initial immune process, M1 macrophages are involved in the primary immune response and subsequently polarize towards the M2 phenotype to play a role in the bone repair process [61]. However, excessive M1 macrophages can exacerbate inflammation and delay the subsequent bone repair process [62–64]. The RT-qPCR results demonstrated that the composite scaffold undergoing the shape memory process effectively induced macrophage M2 polarization, confirming their strong immunomodulatory capability.

The macrophage phenotype regulatory performance of the composite scaffold was further validated using immunofluorescence staining, western blotting, and flow cytometry. The immunofluorescence staining results are shown in Fig. 5E. Consistent with the qPCR results, RAW264.7 cells treated with AF-SP exhibited the strongest green fluorescence (M2 phenotype) and the weakest red fluorescence (M1 phenotype) among all groups, indicating robust M2 polarization. Flow cytometry analysis (Fig. 5F and Figure S16) confirmed that the AF-SP group resulted in the most significant percentage of macrophages exhibiting the M2 phenotype. Western blotting was employed to assess the protein expression levels of CD86 and CD206 in RAW264.7 treated with the composite scaffolds. The results (Figure S17) further supported these findings; the AF-SP group exhibited the highest CD206 and the lowest CD86 protein expression levels, confirming the superior ability of the composite scaffold to induce macrophage M2 polarization. These results demonstrate that the composite scaffold can provide mechanical force stimulation to PVDF to generate charge through a shape memory process, which can effectively promote macrophage M2 polarization, thereby establishing a favorable immune microenvironment for bone repair. Additionally, the composite scaffold achieves in-situ self-power by combining the shape memory process with piezoelectric effects, making it a promising solution for promoting bone defect repair, particularly in patients with limited mobility during the early postoperative stage.

Prior research has demonstrated that M2 macrophages are capable of secreting various cytokines to regulate osteogenesis [59]. Immunofluorescent staining was performed to further assess osteogenic markers secretion levels in RAW264.7 cells co-culture with composite scaffolds. BMP-2 can induce numerous osteogenic gene expression and is vital for bone repair. In contrast, TGF-β1 can facilitate intramembranous osteogenesis [65–68]. As shown in Figure S18, the results revealed that RAW264.7 cells treated with AF-SP demonstrated the highest secretion levels of BMP-2 and TGF-β1. These findings confirm that the composite scaffold, particularly undergoing the shape-memory process, can facilitate macrophage M2 polarization, thereby enhancing osteogenic factors secretion.

Subsequently, to evaluate the immunoregulatory role of the composite scaffold in osteogenesis, RAW264.7 cells were treated with composite scaffolds, and the resulting conditioned medium was collected to culture BMSCs (Figure S19). The results showed that the AF-SP group exhibited the highest alkaline phosphatase (ALP) and Alizarin Red S (ARS) activity. The above findings indicate that the composite scaffold, particularly undergoing the shape memory process, can enhance osteogenesis via immunoregulation.

Mechanistic insights into macrophage polarization induced by the composite scaffold

We have confirmed that the composite scaffold can provide mechanical force stimulation to PVDF to generate charge through a shape memory process and facilitate macrophage M2 polarization. Western blotting analysis was conducted to explore the signaling mechanisms, focusing on the expression of PI3K, P-PI3K, Akt, and

P-Akt in RAW264.7 cells treated with composite scaffolds. Previous reports have highlighted the critical role of the PI3K/Akt signaling pathway in inducing macrophage M2 polarization [69]. Figure S20 illustrates that the AF-SP group exhibited the strongest upregulation of P-PI3K and P-Akt. The results demonstrate that the composite scaffold, particularly undergoing the shape memory process, can activate the Pl3K/Akt signaling pathway to induce macrophage M2 polarization, modulate the immune microenvironment, and promote stem cell osteogenic differentiation.

Biomineralization study of PVDF-SMPU composite scaffold

Piezoelectric characterization results revealed that the composite scaffold can generate negative charges during the shape memory process. Under physiological conditions, these charges can facilitate the formation of a mineralized matrix, which is beneficial for extracellular matrix mineralization [70]. To assess the biomineralization performance of the composite scaffold, samples were immersed in 1.5-fold simulated body fluid (1.5 × SBF) for 7 days. The scaffolds were then retrieved, washed, and dried. The SEM was used to observe surface mineralized components. As shown in Figure S21, the AF-SP group exhibited the thickest mineralized layer, followed by RF-SP. These results indicate that the composite scaffold can provide mechanical force stimulation to PVDF to generate charge through the shape memory process, promoting the formation of the mineralized matrix.

In vitro osteogenic activity of PVDF-SMPU composite scaffold

Patients with bone defects often experience limited mobility and can't provide mechanical force stimulation to the composite scaffold through rehabilitation exercises during the initial postoperative stages. However, once the patients regain exercise ability, continuous mechanical force stimulation can be applied to the composite scaffold to output voltage through rehabilitation exercises (Fig. 6A). To evaluate the voltage output performance of the composite scaffold under continuous mechanical force stimulation, a mechanical impact device was used to impact the composite scaffold repeatedly. By analyzing the stress–strain curve of the scaffold, we found that 2% compressive strain corresponds to a stress of 5 N (Figure S22). Based on piezoelectric characterization results (Figure S1), this stress level can stimulate the PVDF to generate a surface static voltage of − 0.4 kV. Previous studies have shown that the surface static voltage in the range of − 0.1 kV to − 4.9 kV contributed to bone defect repair, indicating that the surface static voltage generated by the composite scaffold is sufficient for bone defect repair [57]. Consequently, the distance between the mechanical lever arm and the scaffold was adjusted so that each impact could induce a 2% compressive strain on the scaffold, with an impact frequency of two cycles per second, simulating the step frequency during human rehabilitation. As shown in Fig. 6B, both AF and RF scaffolds demonstrated stable voltage output under continuous mechanical impact. These results suggest that the patients can provide continuous mechanical force stimulation to the composite scaffold to output voltage through rehabilitation exercises for bone defect repair.

The composite scaffold was co-cultured with BMSCs to assess the osteogenic capacity. Direct mechanical impact on the composite scaffold during cell co-culture could adversely affect the cells, and applying such impacts under culture conditions presents practical challenges. Therefore, an ultrasound therapy device was used to simulate mechanical force stimulation on the composite scaffold (Fig. 6C). Before co-culture experiments, the voltage output performance of the composite scaffold under ultrasound stimulation was assessed. As shown in Fig. 6D and Figure S23, the voltage output increased with increasing ultrasound power. When the power increased to 2 W/cm^2, the output voltage (RF: 1.6 V; AF: 2.1 V) was close to the output voltage under the mechanical impact experiment (RF: 2.2 V; AF: 2.9 V). According to previous studies, these voltage levels are sufficient to meet the requirements for immunoregulation and osteogenesis [11]. Therefore, the ultrasound parameters for the subsequent experiments were set to 2 W/cm^2, 1 MHz, and 20 min/day.

ALP is a key osteogenic marker for cell maturation and mineralization [71, 72]. The ALP staining results (Fig. 6E) showed that the AF-U (AF scaffold stimulated by ultrasound) group and RF-U (RF scaffold stimulated by ultrasound) group exhibited a larger stained area than the

(See figure on next page.)

Fig. 6 In vitro osteogenic differentiation study. **A** Schematic representation of the patient applying mechanical force stimulation to the composite scaffold to output voltage through rehabilitation exercise; **B** The voltage output of composite scaffolds under continuous mechanical impact; **C** Schematic representation of cells culture with scaffolds under ultrasound stimulation; **D** Voltage output of scaffold under ultrasound stimulation (1 MHz, 2 W/cm^2); **E**, **F** ALP and ARS staining results of BMSCs treated with different composite scaffolds (**G**) Expression of osteogenic-related genes in BMSCs cultured with different composite scaffolds. The control group was operated without scaffold treatment. *$p < 0.05$, significant **$p < 0.01$, highly significant (n = 3; error bars represent standard deviation)

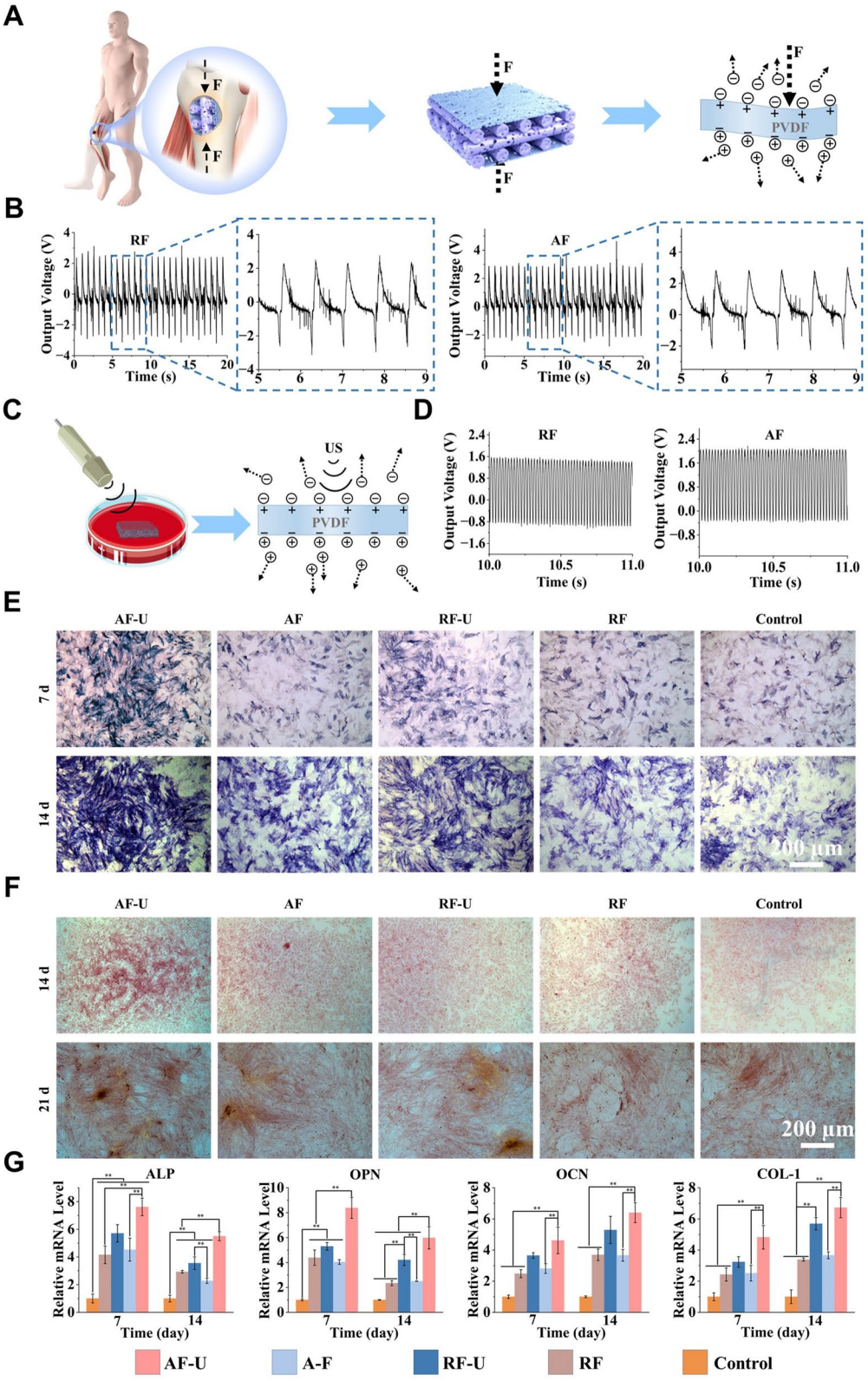

Fig. 6 (See legend on previous page.)

other groups, with the AF-U group showing the largest stained area, indicating the highest ALP expression level. The ALP activity assay results (Figure S24A) further confirmed this observation, as AF-U and RF-U groups demonstrated significantly higher ALP activity, with AF-U displaying the highest activity, consistent with the ALP staining results. ARS staining was conducted to evaluate late-stage extracellular matrix mineralization (Fig. 6F). The results showed that the AF-U and RF-U groups exhibited larger and more intensely stained areas, with the AF-U group displaying the most extensive stained area and deepest color. The quantitative analysis of ARS staining results (Figure S24B) confirmed that AF-U and RF-U groups had significantly higher mineralization levels, with AF-U achieving the highest mineralization levels. These findings demonstrate that the composite scaffold can output voltage under continuous mechanical force stimulation, enhancing ALP expression and facilitating extracellular matrix mineralization, thereby exhibiting excellent osteogenic activity.

RT-qPCR was conducted to assess osteogenic-related gene expression. As shown in Fig. 6G, AF-U and RF-U groups exhibited significantly higher expression levels for both early osteogenic markers (ALP and OPN) and late osteogenic markers (OCN and COL-1), with AF-U showing the highest expression levels across all markers. The above results indicate that the composite scaffold can output voltage under continuous mechanical force stimulation, promoting osteogenic-related gene expression. Previous studies have shown that electrical stimulation can stimulate osteogenic-related gene expression in BMSCs, aligning with the observations from our research [73]. Western blotting analysis further validated the composite scaffold's osteogenic potential. As shown in Figure S25, BMSCs treated with the AF-U and RF-U significantly exhibited higher expression of four osteogenic markers compared to other groups, and the AF-U group displayed the highest expression levels for all four proteins. These findings indicate that the composite scaffold can output voltage under continuous mechanical force stimulation and effectively promote osteogenic-related protein expression in BMSCs. In conclusion, the composite scaffold can output voltage under continuous mechanical force stimulation, promoting osteogenic differentiation of BMSCs and making it an ideal platform for bone regeneration.

In vitro osteogenic-related mechanism study

When BMSCs are exposed to electrical signals, the specific surface receptors can be activated and then promote the transcription of osteogenic genes by activating relevant osteogenic signaling pathways, ultimately promoting osteogenic differentiation [4]. Integrin subtypes are a group of cell surface receptors, among which integrin α1, α2, α5, and β1 play crucial roles in cell adhesion and osteogenic differentiation [74]. Once activated, they can trigger corresponding signaling pathways to enhance osteogenic gene and protein expression. Figure S26A showed that BMSCs treated with AF-U and RF-U exhibited significantly higher expression levels of integrin α1, α2, α5, and β1, with the AF-U group displaying the highest expression levels. These results suggest that the composite scaffold can deliver electrical stimulation under continuous mechanical force stimulation, enhancing integrin gene expression in BMSCs. The integrin α2β1 can activate the FAK signaling pathway, leading to the phosphorylation of Runx2, while integrin α1β1 can interact with type IV collagen and influence osteogenic differentiation [75, 76]. Furthermore, integrin α5 can promote osteogenic differentiation by activating the FAK/ERK1/2-MAPKs and PI3K signaling pathways [77]. Therefore, after confirming that the composite scaffold can activate integrin-related receptors of BMSCs, the activation of signaling pathways related to stem cell osteogenic differentiation was investigated. Figure S26B showed that the AF-U and RF-U groups exhibited higher P-FAK and P-ERK protein expression levels than other groups, with the AF-U group achieving the highest expression levels. These findings demonstrate that the composite scaffold can activate integrin-related receptors on the surface of BMSCs through in-situ electric stimulation, triggering the FAK/ERK signaling pathway and ultimately enhancing osteogenic gene transcription in BMSCs.

In vivo bone defect repair performance evaluation of PVDF-SMPU composite scaffold

The rat femoral defect model was used to assess the composite scaffold's bone defect repair performance in vivo. To simulate the limited mobility experienced by patients during the early postoperative period, rats were placed in cages to restrict movement immediately after scaffold implantation at the defect site. After 3 days, the rats were allowed unrestricted movement to mimic patient rehabilitation exercises (Fig. 7A).

The experimental groups were categorized as follows: AF-SP: A-PVDF-SMPU composite scaffolds (3 mm diameter, 2 mm height), compressed and fixed to 2 mm in diameter, and experienced shape memory process after implantation in the defect site; AF: A-PVDF-SMPU composite scaffolds (3 mm diameter, 2 mm height), this composite scaffold was not experienced shape memory process after implantation in the defect site; RF-SP: R-PVDF-SMPU composite scaffolds (3 mm diameter, 2 mm height), compressed and fixed to 2 mm in diameter, and experienced shape memory process after implantation in the defect site; RF: R-PVDF-SMPU composite

scaffolds (3 mm diameter, 2 mm height), the composite scaffold was not experienced shape memory process after implantation in the defect site; control group (no composite scaffolds). The composite scaffold can be implanted with minimally invasive procedures due to its excellent shape memory performance. Under physiological temperature, the composite scaffold can recover its original size, providing mechanical force stimulation to PVDF and generating charge. These charges contributed to immune microenvironment regulation during the early postoperative phase. After 3 days, unrestricted movement of the rats provided further continuous mechanical force stimulation to the composite scaffold, enabling sustained voltage output to promote bone regeneration.

Micro-CT analysis was performed to evaluate femoral defect repair. Because the cylindrical femoral defect was constructed with a diameter of 3 mm and a depth of 2 mm. When analyzing the micro-CT results, we delineated a cylindrical region with a diameter of 3 mm and a depth of 2 mm at the defect site and quantified the volume of new bone by calculating the ratio of bone volume within this region to total volume. Figure 7B and Figure S27A are the reconstructed sagittal and cross-sectional images, and the green area represents the new bone. Because the volume of new bone was relatively limited in the fourth week and a small amount of new bone formation was also observed in the control group, the differences between groups were small. However, it was still revealed that the AF-SP group achieved the highest levels of bone regeneration. This result confirms that the composite scaffolds could generate charge through the shape memory process of the scaffold and rehabilitation exercises of patients to promote bone defect repair, achieving in-situ electricity stimulation in the form of self-power. Quantitative analysis of micro CT results (Fig. 7C, D) further confirmed these findings. Although previous studies have shown that the degradability of scaffolds negatively affects their continuous electrical stimulation performance [21], the degradation rate of the composite scaffold prepared in this study was relatively slow (Figure S7), which can avoid the rapid decline of continuous piezoelectric stimulation performance caused by rapid degradation. The micro CT results proved that the composite scaffold had a good bone defect repair effect, indicating that the composite scaffold can meet the needs of bone defect repair even though the degradation of the composite scaffold may have a negative impact on the sustainable piezoelectric stimulation performance of the scaffold. These results demonstrate that the scaffolds can generate charge through the shape memory process of the scaffold and rehabilitation exercises of patients to promote bone defect repair, providing a self-powered platform that effectively promotes bone defect repair. More importantly, this dual-phase mechanism, involving early immune microenvironment regulation and continuous electrical stimulation during rehabilitation exercise, highlights the composite scaffold's potential in bone regeneration.

Histological staining evaluation was performed on decalcified femur sections to access new bone formation and biocompatibility. H&E staining results (Fig. 7E and Figure S27B) showed no signs of inflammation, fibrotic reactions, or pathological abnormalities across all experimental groups. For the new bone formation, because the color depth and uniformity of staining may be affected by sample processing, staining time, or dye concentration, visual differences were smaller, but it was still observed that the AF-SP group showed the highest new bone formation. Quantitative analysis of the H&E staining result in Figure S28A showed that the AF-SP group had the most new bone area, and the RF-SP group also had more new bone area, consistent with the staining results and Micro CT results, which proved that the composite scaffold could continuously apply piezoelectric stimulation to the defect site through shape memory process and rehabilitation exercise, promote bone defect repair. Furthermore, no inflammatory signs were found in major organs (Figure S29), demonstrating the composite scaffold's excellent biocompatibility. Masson's trichrome staining (Fig. 7E and Figure S27B) revealed that the AF-SP group had the most collagen deposition and new bone formation. In contrast, the other three groups exhibited minimal collagen deposition and limited new bone formation. Quantitative analysis of Masson's trichrome staining result in Figure S28B showed that the AF-SP group had the most new bone area, and the RF-SP group also had more new bone area, consistent with the staining results and Micro-CT results. The above findings confirm that the composite scaffold can achieve in-situ electric stimulation through the shape memory process of scaffold

(See figure on next page.)

Fig. 7 In vivo evaluation of bone defect repair. **A** The scaffold implantation process and experiment design; **B**–**D** Reconstructed three-dimensional micro-CT images of the rat skull (the green area represented the new bone) and the regenerated bone's bone volume fraction (BV/TV) and bone mineral density (BMD) values. **E** Histological evaluation using H&E staining and Masson trichrome staining. S: residual scaffold; FCT: fibrous connective tissue; HB: host bone; NB: new bone. The control group was operated without scaffold treatment. $^{**}p < 0.01$, highly significant ($n = 4$, error bars represent standard deviation)

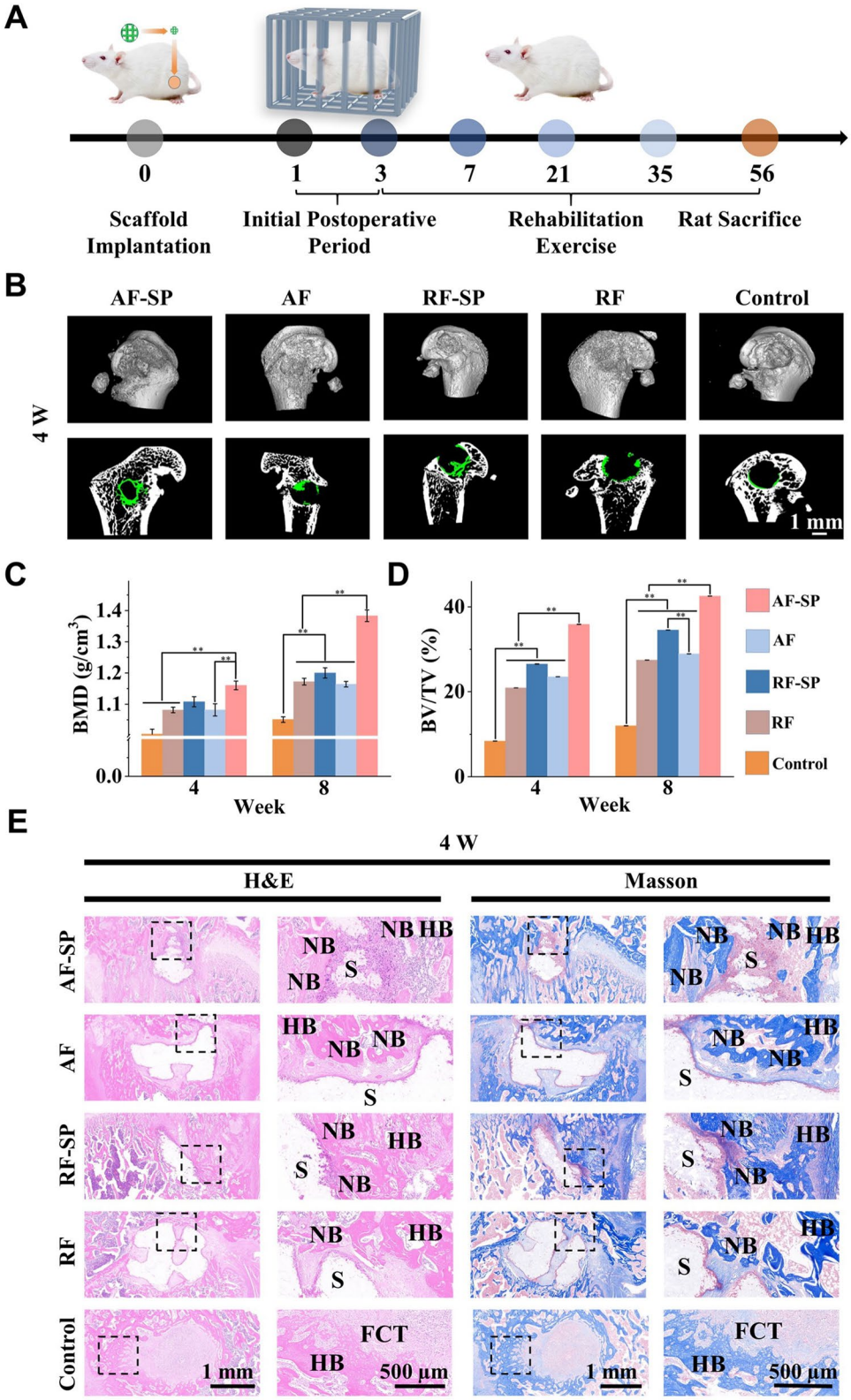

Fig. 7 (See legend on previous page.)

and rehabilitation exercises of patients to promote bone repair effectively.

Immunofluorescence and immunohistochemistry staining were conducted to assess osteogenic-related marker (OPN and OCN) expression in vivo. The immunofluorescence staining results are shown in Figure S30A-F, with green representing OPN and red representing OCN. The results demonstrated that the AF-SP group had the most intense fluorescence, indicating robust secretion of osteogenic factors. The immunohistochemistry staining results are shown in Figure S30G, where the brown areas indicate positive protein expression, with darker color representing higher protein expression levels. The results demonstrated that the AF-SP and RF-SP groups exhibited larger brown-stained areas than the other three groups, with the AF-SP group presenting the most extensive positive staining. The above results confirm that the composite scaffold can stimulate osteogenic marker expression in vivo through in-situ electric stimulation, demonstrating outstanding osteogenic activity and bone repair performance.

Previous research indicates that the initial inflammatory response after scaffold implantation plays a vital role in bone repair [78, 79]. However, prolonged inflammation significantly delays bone healing, ultimately leading to poor repair results [62, 63]. The phenotypic transformation of macrophages from M1 to M2 is essential for reducing inflammation in the bone regeneration process [58, 80]. Immunohistochemistry and immunofluorescence staining were performed to assess the macrophage phenotypic transformation in vivo. The immunofluorescence staining results are shown in Figure S31A-F. The results revealed that the AF-SP group exhibited the strongest green fluorescence (CD206) and the weakest red fluorescence (iNOS) among all groups, and the RF-SP group also showed a higher green fluorescence and lower red fluorescence than the remaining three groups. This result suggests that the composite scaffold can induce macrophage M2 polarization through in-situ electric stimulation. Immunohistochemistry staining (Figure S31G) further supported these results, with the AF-SP and RF-SP groups demonstrating significantly higher CD206 expression and lower iNOS expression, as evidenced by darker brown staining for CD206 and lighter staining for iNOS. Importantly, no significant inflammatory reaction occurred in all experimental groups, confirming the excellent in vivo biocompatibility of the composite scaffolds. These findings suggest that through in-situ self-power, the composite scaffold can effectively induce macrophage M2 polarization. This transition alleviates the early inflammatory response following scaffold implantation and creates a conducive environment for subsequent bone repair.

Although our study successfully developed a 3D-printed shape-memory piezoelectric bone repair scaffold with in-situ self-power capabilities and demonstrated its excellent bone repair effect in subsequent in vitro and in vivo experiments, there are still some limitations. First, the scaffold will gradually degrade over time in vivo. While this is necessary for bone defect repair scaffolds, it inevitably negatively impacts the sustained piezoelectric output induced by structural changes. Although the biodegradable composite scaffold achieved a good repair effect of bone defect in this study, it is foreseeable that resolving the contradiction between scaffold degradation and sustainable piezoelectric output could lead to an even better bone repair effect.

Second, the long-term toxicity of the scaffold in vivo has not been adequately investigated. The degradation of biodegradable materials in vivo is a prolonged process, and the metabolism, distribution, and long-term toxicity of their degradation products need to be adequately investigated, as this is crucial for further applications [81]. This study has only demonstrated that the scaffold did not cause significant inflammatory responses in major organs during the 8 weeks post-implantation but did not sufficiently investigate the metabolism, distribution, and long-term toxicity of its degradation products. Therefore, future work will focus on enhancing the investigation of the long-term toxicity of the composite scaffold in vivo.

Conclusion

This study successfully developed an in-situ self-powered 3D printed composite scaffold with exceptional shape memory performance, piezoelectric properties, biocompatibility, immune modulation, and osteogenic properties. The shape memory activation temperature of the composite scaffold is 33 ℃, enabling it to undergo a shape recovery process at physiological temperatures. More importantly, the composite scaffold achieves a perfect combination of shape memory process and piezoelectric effect during the bone repair process. The composite scaffold utilizes its shape memory behavior to provide mechanical force stimulation to PVDF to generate a charge, which can modulate the local immune microenvironment during the initial postoperative stage when the patients have limited mobility. As patients regain mobility, they can apply continuous mechanical force stimulation to the composite scaffold through rehabilitation exercises, enabling sustained voltage output to promote bone repair further. This dual-stage functionality allows the scaffold to achieve in-situ self-power throughout the entire bone healing process. Both in vitro and in vivo experiments demonstrate the excellent immune modulation and osteogenic performance of the composite

scaffold. In summary, this innovative scaffold integrates outstanding shape memory behavior, in-situ self-power, immune modulation, and osteogenic properties, offering a highly promising platform for bone tissue engineering.

Supplementary Information

The online version contains supplementary material available at https://doi.org/10.1186/s12951-025-03325-x.

Supplementary Material 1. **Experimental Section.** (**1**. Biomineralization of PVDF@SMPU composite scaffolds; **2**. In vitro biocompatibility of PVDF@SMPU composite scaffolds; **3**. In vitro osteogenic differentiation performance evaluation of PVDF@SMPU composite scaffolds; **4**. Osteogenic-related signaling pathways; **5**. In vitro macrophage phenotype regulation performance evaluation of PVDF@SMPU composite scaffolds; **6**. In vivo bone defect repair performance evaluation of PVDF@SMPU composite scaffolds) and **additional data** (**Figure** S1. (A) Surface electrostatic voltage of PVDF nanofibers under different mechanical forces. (B) Surface electrostatic voltage of PVDF nanofibers under different ultrasound power.; **Figure** S2. The output voltage of the PVDF under different bending Angle ((A): arranged fibers; (B): random fibers); **Figure** S3. The preparation process for SMPU; **Figure** S4. The FTIR spectrum of SMPU; **Figure** S5. The pictures of the SMPU with the PCL: castor oil molar ratios of 1:0.8 and 1:1.2 at the maximum tensile strain; **Figure** S6. The work output of SMPU with the PCL: castor oil molar ratios of 1:0.8 and 1:1.2 during the shape recovery process; **Figure** S7. The hydrolytic degradation of the composite scaffold over 7 days; **Figure** S8. Exploring ink ratios for scaffold printing; **Figure** S9. Macroscopic and microscopic images of scaffolds before and after the removal of sodium chloride; **Figure** S10. The shape fixity rate (Sf) and shape recovery rate (Sr) of the composite scaffolds; **Figure** S11. In vitro simulation of SMPU scaffolds for the minimally invasive implantation and shape memory process; **Figure** S12. The water contact angle of composite scaffolds; **Figure**. S13. The quantitative analysis results of live/dead fluorescent staining (A, B) and immunofluorescence staining (C). The control group was operated without scaffold treatment. *$p < 0.05$, significant **$p < 0.01$, highly significant ($n = 3$, error bars represent standard deviation); **Figure** S14. The hemolysis test of the composite scaffold; **Figure** S15. Cell scratch assay results after incubation for 0 and 48 h with different scaffolds; **Figure** S16. The quantitative analysis of flow cytometry result; **Figure** S17. the protein expression levels of CD86 and CD206 in macrophages treated with the scaffolds; **Figure** S18. Immunofluorescence staining results of bone-related genes (BMP-2 and TGF-β1) expression in RAW264.7 cells cultured on different scaffolds for 4 days; **Figure** S19. In vitro study of stem cell osteogenesis differentiation using ALP (A) and ARS (B) staining in macrophage conditioned medium; *$p < 0.05$, significant **$p < 0.01$, highly significant ($n = 3$); **Figure** S20. In vitro macrophage M2 polarization mechanisms: The expression of PI3K/Akt signaling pathway-related proteins in RAW264.7 cultured on different scaffolds after 24 h; **Figure** S21. SEM image and mapping of surface mineralization components of composite scaffolds after simulated body fluid treatment; **Figure** S22. Residual stress of the scaffold under different levels of residual strain; **Figure** S23. Voltage output of PVDF at different ultrasound powers (1 MHz) ((A-C): AF; (D-F): RF); **Figure** S24. The quantitative analysis of ALP and ARS staining results; **Figure** S25. The expression of osteogenic-related proteins; **Figure** S26. In vitro study of osteogenesis related signaling pathway. (A) The expression of integrin subtypes-related genes in BMSCs cultured on different scaffolds after 6 h. (B) The expression of osteogenic signaling pathway-related proteins in BMSCs cultured on different scaffolds after 24 h.; *$p < 0.05$, significant **$p < 0.01$, highly significant ($n = 3$); **Figure** S27. (A) Reconstructed three-dimensional micro-CT images of the rat skull at 8 weeks. (B) Histological evaluation by HE staining and Masson trichrome staining at 8 weeks. S indicates the location of the residual scaffold, FCT indicates fibrous connective tissue, HB indicates host bone, and NB indicates new bone. **$p < 0.01$, highly significant ($n = 4$); **Figure**. S28. The quantitative analysis of the H&E staining (A) and Masson's trichrome staining (B) result; **Figure** S29. H&E staining images of various organs (including heart, liver, spleen, lung, and kidney); **Figure** S30. (A-F) immunofluorescent staining of OPN and OCN in the tissues around the scaffolds at 4 and 8 weeks post-operation (blue: nucleus; green: OCN maker; red: OPN marker).; (G) immunohistochemistry staining of OPN and OCN in the tissues around the scaffolds at 4 and 8 weeks post-operation; **Figure** S31. (A-F) immunofluorescent staining of CD206 and iNOS in the tissues around the scaffolds at 4 and 8 weeks post-operation (blue: nucleus; green: CD206 maker; red: iNOS marker).; (G) immunohistochemistry staining of CD206 and iNOS in the tissues around the scaffolds at 4 and 8 weeks post-operation; **Table 1**. Primers designed for genes related to osteogenic differentiation of BMSCs and immune response of RAW264.7 cells).

Acknowledgements
Not applicable.

Author contributions
B. L.: conceptualization, investigation, methodology, writing original draft, validation, data curation. Y. C. M.: performed Molecular biology and cell biology experiments. B. L., K. F., and X. J. Z: co-wrote the manuscript. X. G., S. C and C. L. H: conceptualization, writing-review & editing, supervision, funding acquisition. All authors reviewed the manuscript.

Funding
This work was financially supported by the National Natural Science Foundation of China (32271412, 32071350, 32171404), Natural Science Foundation of Shanghai (21ZR1403100) and Science and Technology Commission of Shanghai Municipality (20DZ2254900).

Data availability
Data is provided within the manuscript or supplementary information files.

Declarations

Ethics approval and consent to participate
All the experimental animal procedures were performed by following local animal welfare laws and guidelines and approved by the Animal Ethics Committee of Donghua University (No: DHUEC-NSFC-2022–27, Date: March 1, 2022).

Consent for publication
Not applicable.

Competing interests
The authors declare no competing interests.

Author details
[1]State Key Laboratory for Modification of Chemical Fibers and Polymer Materials, College of Biological Science and Medical Engineering, Donghua University, Shanghai 201620, People's Republic of China. [2]Department of Orthopedics, Shanghai General Hospital, Shanghai Jiao Tong University School of Medicine, Shanghai 200080, China. [3]Department of Orthopaedics, Tongren Hospital, Shanghai Jiao Tong University School of Medicine, Shanghai 200336, People's Republic of China. [4]State Key Laboratory of Molecular Engineering of Polymers, Fudan University, Shanghai 200433, China.

Received: 20 January 2025 Accepted: 13 March 2025
Published online: 24 March 2025

References

1. Chen S, Yu Y, Xie S, Liang D, Shi W, Chen S, Li G, Tang W, Liu C, He Q. Local H_2 release remodels senescence microenvironment for improved repair of injured bone. Nat Commun. 2023;14:7783–7783.
2. Su N, Villicana C, Yang F. Immunomodulatory strategies for bone regeneration: a review from the perspective of disease types. Biomaterials. 2022;286: 121604.

3. Chen L, Yang J, Cai Z, Huang Y, Xiao P, Wang J, Wang F, Huang W, Cui W, Hu N. Electroactive biomaterials regulate the electrophysiological microenvironment to promote bone and cartilage tissue regeneration. Adv Funct Mater. 2024;34:2314079.
4. Mao L, Bai L, Wang X, Chen X, Zhang D, Chen F, Liu C. Enhanced cell osteogenesis and osteoimmunology regulated by piezoelectric biomaterials with controllable surface potential and charges. ACS Appl Mater. 2022;14:44111–24.
5. Li Y, Fan Y, Zhao S, Cheng B. Ultrasound-triggered piezoelectric polyetheretherketone with boosted osteogenesis via regulating Akt/GSK3β/β-catenin pathway. J Nanobiotechnol. 2024;22:539.
6. Zhou S, Xiao C, Fan L, Yang J, Ge R, Cai M, Yuan K, Li C, Crawford RW, Xiao Y, et al. Injectable ultrasound-powered bone-adhesive nanocomposite hydrogel for electrically accelerated irregular bone defect healing. J Nanobiotechnol. 2024;22:54.
7. Wang L, Chen K, Fan Y, Yin L. Novel implantable devices delivering electrical cues for tissue regeneration and functional restoration. Med Novel Technol Devices. 2022;16: 100146.
8. Li Y, Luo Y, Deng H, Shi S, Tian S, Wu H, Tang J, Zhang C, Zhang X, Zha J-W, Xiao S. Advanced dielectric materials for triboelectric nanogenerators: principles, methods, and applications. Adv Mater. 2024;36:2314380.
9. Wang A, Ma X, Yang Y, Shi G, Han L, Hu X, Shi R, Yan J, Guo Q, Zhao Y. Biophysical-driven piezoelectric and aligned nanofibrous scaffold promotes bone regeneration by re-establishing physiological electrical microenvironment. Nano Res. 2024;17:2–18.
10. Hong J, Wei X, Zhang H, Xiao Y, Meng C, Chen Y, Li J, Li L, Lee S, Shi Q, Wu J. Advances of triboelectric and piezoelectric nanogenerators toward continuous monitoring and multimodal applications in the new era. Int J Extreme Manuf. 2025;7: 012007.
11. Pi W, Rao F, Cao J, Zhang M, Chang T, Han Y, Zheng Y, Liu S, Li Q, Sun X, Shao Y. Sono-electro-mechanical therapy for peripheral nerve regeneration through piezoelectric nanotracts. Nano Today. 2023;50: 101860.
12. Wu H, Shi S, Zhou H, Zhi C, Meng S, Io W-F, Ming Y, Wang Y, Lei L, Fei B, et al. Stem cell self-triggered regulation and differentiation on polyvinylidene fluoride electrospun nanofibers. Adv Funct Mater. 2023;34:2309270.
13. Huang Y, Wan X, Su Q, Zhao C, Cao J, Yue Y, Li S, Chen X, Yin J, Deng Y, et al. Ultrasound-activated piezo-hot carriers trigger tandem catalysis coordinating cuproptosis-like bacterial death against implant infections. Nat Commun. 2024;15:1643.
14. Ma J, Yuan M, Yang Z, Ma Z, Zhang J, Li Z, Pa M, Cheng Z, Lin J. Surface oxygen vacancies and corona polarization of $Bi_4Ti_3O_{12}$ nanosheets for synergistically enhanced sonopiezoelectric therapy. J Am Chem Soc. 2024;146:22348–59.
15. Ricotti L, Cafarelli A, Manferdini C, Trucco D, Vannozzi L, Gabusi E, Fontana F, Dolzani P, Saleh Y, Lenzi E, et al. Ultrasound stimulation of piezoelectric nanocomposite hydrogels boosts chondrogenic differentiation in vitro, in both a normal and inflammatory milieu. ACS Nano. 2024;18:2047–65.
16. Wang X, Guo X, Ren H, Song X, Chen L, Yu L, Ren J, Chen Y. An "Outer Piezoelectric and Inner Epigenetic" logic-gated PANoptosis for osteosarcoma sono-immunotherapy and bone regeneration. Adv Mater. 2024;37:2415814.
17. Wang T, Ouyang H, Luo Y, Xue J, Wang E, Zhang L, Zhou Z, Liu Z, Li X, Tan S, et al. Rehabilitation exercise-driven symbiotic electrical stimulation system accelerating bone regeneration. Sci Adv. 2024;10: eadi6799.
18. Niu Q, Wei H, Hsiao BS, Zhang Y. Biodegradable silk fibroin-based bio-piezoelectric/triboelectric nanogenerators as self-powered electronic devices. Nano Energy. 2022;96: 107101.
19. Zhang J, Yang T, Tian G, Lan B, Deng W, Tang L, Ao Y, Sun Y, Zeng W, Ren X, et al. Spatially confined MXene/PVDF nanofiber piezoelectric electronics. Adv Fiber Mater. 2024;6:133–44.
20. Huang A, Zhu Y, Peng S, Tan B, Peng X. Improved energy harvesting ability of single-layer binary fiber nanocomposite membrane for multifunctional wearable hybrid piezoelectric and triboelectric nanogenerator and self-powered sensors. ACS Nano. 2023;18:691–702.
21. Luo B, Wang S, Song X, Chen S, Qi Q, Chen W, Deng X, Ni Y, Chu C, Zhou G, et al. An encapsulation-free and hierarchical porous triboelectric scaffold with dynamic hydrophilicity for efficient cartilage regeneration. Adv Mater. 2024;34:2401009.
22. Feng P, Zhao R, Tang W, Yang F, Tian H, Peng S, Pan H, Shuai C. Structural and functional adaptive artificial bone: materials, fabrications, and properties. Adv Funct Mater. 2023;33:2214726.
23. Hardy JG, Palma M, Wind SJ, Biggs MJ. Responsive biomaterials: advances in materials based on shape-memory polymers. Adv Mater. 2016;28:5717–24.
24. Kalogeropoulou M, Diaz-Payno PJ, Mirzaali MJ, van Osch GJVM, Fratila-Apachitei LE, Zadpoor AA. 4D printed shape-shifting biomaterials for tissue engineering and regenerative medicine applications. Biofabrication. 2024;16: 022002.
25. Wang C, Yue H, Liu J, Zhao Q, He Z, Li K, Lu B, Huang W, Wei Y, Tang Y, Wang M. Advanced reconfigurable scaffolds fabricated by 4D printing for treating critical-size bone defects of irregular shapes. Biofabrication. 2020;12: 045025.
26. Li G, Li Z, Min Y, Chen S, Han R, Zhao Z. 3D-printed piezoelectric scaffolds with shape memory polymer for bone regeneration. Small. 2023;19:2302927.
27. Zhang Y, Li C, Zhang W, Deng J, Nie Y, Du X, Qin L, Lai Y. 3D-printed NIR-responsive shape memory polyurethane/magnesium scaffolds with tight-contact for robust bone regeneration. Bioact Mater. 2022;16:218–31.
28. Li M, Chen K, Zhang D, Ye Z, Yang Z, Wang Q, Jiang Z, Zhang Y, Shang Y, Cao A. Wet-spinning carbon nanotube/shape memory polymer composite fibers with high actuation stress and predesigned shape change. Adv Sci. 2024;11:2404913.
29. Lv Z, Wu Y, Lin J, Li W, Weisbecker H, Wang P, Song X, Sun W, Sun Z, Xie Y, et al. Schottky heterojunction facilitates osteosarcoma ferroptosis and enhances bone formation in a switchable mode. Adv Funct Mater. 2024;34:2312032.
30. Liu D, Wang X, Gao C, Zhang Z, Wang Q, Pei Y, Wang H, Tang Y, Li K, Yu Y, et al. Biodegradable piezoelectric-conductive integrated hydrogel scaffold for repair of osteochondral defects. Adv Mater. 2024;36:2409400.
31. Lee JC, Park CH, Kim CS. Amplified piezoelectric response with 13-phase formation in PVDF blended 3D cotton type nanofibers for osteogenic differentiation. J Ind Eng Chem. 2023;118:155–63.
32. Adadi N, Yadid M, Gal I, Asulin M, Feiner R, Edri R, Dvir T. Electrospun fibrous PVDF-TrFe scaffolds for cardiac tissue engineering, differentiation, and maturation. Adv Mater Technol. 2020;5:1900820.
33. Meng N, Ren X, Santagiuliana G, Ventura L, Zhang H, Wu J, Yan H, Reece MJ, Bilotti E. Ultrahigh β-phase content poly(vinylidene fluoride) with relaxor-like ferroelectricity for high energy density capacitors. Nat Commun. 2019;10:4535.
34. Wu L, Jin Z, Liu Y, Ning H, LiuAlamusi X, Hu N. Recent advances in the preparation of PVDF-based piezoelectric materials. Nanotechnol Rev. 2022;11:1386–407.
35. Feng Z, Zhao Z, Liu Y, Liu Y, Cao X, Yu D-G, Wang K. Piezoelectric effect polyvinylidene fluoride (PVDF): from energy harvester to smart skin and electronic textiles. Adv Mater Technol. 2023;8:2300021.
36. Li L, Peng F, Zheng G, Dai K, Liu C, Shen C. Electrospun core-sheath PVDF piezoelectric fiber for sensing application. ACS Appl Mater. 2023;15:15938–45.
37. Liu Z, Cai M, Zhang X, Yu X, Wang S, Wan X, Wang ZL, Li L. Cell-traction-triggered on-demand electrical stimulation for neuron-like differentiation. Adv Mater. 2021;33:2106317.
38. Zhang L, Li S, Zhu Z, Rui G, Du B, Chen D, Huang Y-F, Zhu L. Recent progress on structure manipulation of poly(vinylidene fluoride)-based ferroelectric polymers for enhanced piezoelectricity and applications. Adv Funct Mater. 2023;33:2301302.
39. Ren J-Y, Ouyang Q-F, Ma G-Q, Li Y, Lei J, Huang H-D, Jia L-C, Lin H, Zhong G-J, Li Z-M. Enhanced dielectric and ferroelectric properties of poly(vinylidene fluoride) through annealing oriented crystallites under high pressure. Macromolecules. 2022;55:2014–27.
40. Qiu X, Bian Y, Mei X, Luo X, Hu Z, Xuan F-Z, Xiang Y, Zhu G. Fully transparent flexible piezoelectric sensing materials based on electrospun PVDF and their device applications. Adv Mater Technol. 2024;9:2301494.
41. Vijayakanth T, Shankar S, Finkelstein-Zuta G, Rencus-Lazar S, Gilead S, Gazit E. Perspectives on recent advancements in energy harvesting, sensing and bio-medical applications of piezoelectric gels. Chem Soc Rev. 2023;52:6191–220.
42. Choi KK, Park SH, Oh KW, Kim SH. Effect of castor oil/polycaprolactone hybrid polyols on the properties of biopolyurethane. Macromol Res. 2015;23:333–40.

43. Zeng Y, Chen Y, Sha D, Wu Y, Qiu R, Liu W. Highly stretchable fatty acid chain-dangled thermoplastic polyurethane elastomers enabled by H-bonds and molecular chain entanglements. ACS Sustain Chem Eng. 2022;10:11524–32.
44. Sun Y, Tian X, Xie H, Shi B, Zhong J, Liu X, Yang Y. Reprocessable and degradable bio-based polyurethane by molecular design engineering with extraordinary mechanical properties for recycling carbon fiber. Polymer. 2022;258: 125313.
45. Abbasi A, Sadeghi GMM, Ghasemi I, Shahrousvand M. Shape memory performance of green in situ polymerized nanocomposites based on polyurethane/graphene nanoplatelets: synthesis, properties, and cell behavior. Polym Composite. 2018;39:4020–33.
46. Wang C, Wang L, Zhang Z, Zhang N, Huang Y. Water-driven shape memory nanocomposite fibers for actuators. Polym Composite. 2023;44:4215–26.
47. Yu K, Xie T, Leng J, Ding Y, Qi HJ. Mechanisms of multi-shape memory effects and associated energy release in shape memory polymers. Soft Matter. 2012;8:5687–95.
48. Chen J, Wang Z, Yao B, Geng Y, Wang C, Xu J, Chen T, Jing J, Fu J. Ultra-highly stiff and tough shape memory polyurea with unprecedented energy density by precise slight cross-linking. Adv Mater. 2024;36:2401178.
49. Xie R, Hu J, Ng F, Tan L, Qin T, Zhang M, Guo X. High performance shape memory foams with isocyanate-modified hydroxyapatite nanoparticles for minimally invasive bone regeneration. Ceram Int. 2017;43:4794–802.
50. Xue G, Zhang Y, Xie T, Zhang Z, Liu Q, Li X, Gou X. Cell adhesion-mediated piezoelectric self-stimulation on polydopamine-modified poly (vinylidene fluoride) membranes. ACS Appl Mater. 2021;13:17361–71.
51. Cheng Y, Pang SW. Effects of nanopillars and surface coating on dynamic traction force. Microsyst Nanoeng. 2023;9:2–14.
52. Wu H, Dong H, Tang Z, Chen Y, Liu Y, Wang M, Wei X, Wang N, Bao S, Yu D, et al. Electrical stimulation of piezoelectric $BaTiO_3$ coated Ti6Al4V scaffolds promotes anti-inflammatory polarization of macrophages and bone repair via MAPK/JNK inhibition and OXPHOS activation. Biomaterials. 2023;293: 121990.
53. Sun L, Chen X, Ma K, Chen R, Mao Y, Chao R, Wang H, Yu B, Wang J, Zhang S. Novel titanium implant: a 3D multifunction architecture with charge-trapping and piezoelectric self-stimulation. Adv Healthc Mater. 2023;13:2202620.
54. Zheng T, Yu Y, Pang Y, Zhang D, Wang Y, Zhao H, Zhang X, Leng H, Yang X, Cai Q. Improving bone regeneration with composites consisting of piezoelectric poly(L-lactide) and piezoelectric calcium/manganese co-doped barium titanate nanofibers. Compos Part B-Eng. 2022;234: 109734.
55. Orrego S, Chen Z, Krekora U, Hou D, Jeon S-Y, Pittman M, Montoya C, Chen Y, Kang SH. Bioinspired materials with self-adaptable mechanical properties. Adv Mater. 2020;32:1906970.
56. Zhang X, Zhang C, Lin Y, Hu P, Shen Y, Wang K, Meng S, Chai Y, Dai X, Liu X, et al. Nanocomposite membranes enhance bone regeneration through restoring physiological electric microenvironment. ACS Nano. 2016;10:7279–86.
57. Qiao Z, Lian M, Liu X, Zhang X, Han Y, Ni B, Xu R, Yu B, Xu Q, Dai K. Electreted sandwich membranes with persistent electrical stimulation for enhanced bone regeneration. ACS Appl Mater. 2022;14:31655–66.
58. Wu L, Xu Y, Xi K, Gu Y, Tang J, Xin T, Yang H, Wang L, Cui W, Chen L. Regulation of macrophage subtype via injectable micro/nano-structured porous microsphere for reprogramming osteoimmune microenvironment. Chem Eng J. 2022;439: 135692.
59. Zhu Y, Liang H, Liu X, Wu J, Yang C, Wong TM, Kwan KYH, Cheung KMC, Wu S, Yeung KWK. Regulation of macrophage polarization through surface topography design to facilitate implant-to-bone osteointegration. Sci Adv. 2021;7:1–13.
60. Schlundt C, Fischer H, Bucher CH, Rendenbach C, Duda GN, Schmidt-Bleek K. The multifaceted roles of macrophages in bone regeneration: a story of polarization, activation and time. Acta Biomater. 2021;133:46–57.
61. Zhang B, Su Y, Zhou J, Zheng Y, Zhu D. Toward a better regeneration through implant-mediated immunomodulation: harnessing the immune responses. Adv Sci. 2021;8:2100446.
62. Liu S, Wang W, Wu P, Chen Z, Pu W, Li L, Li G, Zhang J, Song J. Pathogenesis-guided engineering of multi-bioactive hydrogel co-delivering inflammation-resolving nanotherapy and pro-osteogenic protein for bone regeneration. Adv Funct Mater. 2023;33:2301523.
63. Wang Y, Lin Q, Zhang H, Wang S, Cui J, Hu Y, Liu J, Li M, Zhang K, Zhou F, et al. M2 macrophage-derived exosomes promote diabetic fracture healing by acting as an immunomodulator. Bioact Mater. 2023;28:273–83.
64. Zhang J, Tong D, Song H, Ruan R, Sun Y, Lin Y, Wang J, Hou L, Dai J, Ding J, Yang H. Osteoimmunity-regulating biomimetically hierarchical scaffold for augmented bone regeneration. Adv Mater. 2022;34:2202044.
65. Ren S, Tang X, Liu L, Meng F, Yang X, Li N, Zhang Z, Aimaijiang M, Liu M, Liu X, et al. Reinforced blood-derived protein hydrogels enable dual-level regulation of bio-physiochemical microenvironments for personalized bone regeneration with remarkable enhanced efficacy. Nano Lett. 2022;22:3904–13.
66. Lu G, Xu Y, Liu Q, Chen M, Sun H, Wang P, Li X, Wang Y, Li X, Hui X, et al. An instantly fixable and self-adaptive scaffold for skull regeneration by autologous stem cell recruitment and angiogenesis. Nat Commun. 2022;13:2499.
67. Wang C, Yue H, Huang W, Lin X, Xie X, He Z, He X, Liu S, Bai L, Lu B, et al. Cryogenic 3D printing of heterogeneous scaffolds with gradient mechanical strengths and spatial delivery of osteogenic peptide/TGF-β1 for osteochondral tissue regeneration. Biofabrication. 2020;12: 025030.
68. Grottkau BE, Hui Z, Ran C, Pang Y. Fabricating vascularized, anatomically accurate bone grafts using 3D bioprinted sectional bone modules, in-situ angiogenesis, BMP-2 controlled release, and bioassembly. Biofabrication. 2024;16: 045008.
69. Li L, Jiang W, Yu B, Liang H, Mao S, Hu X, Feng Y, Xu J, Chu L. Quercetin improves cerebral ischemia/reperfusion injury by promoting microglia/macrophages M2 polarization via regulating PI3K/Akt/NF-κB signaling pathway. Biomed Pharmacother. 2023;168: 115653.
70. Li L, Li Q, Gui L, Deng Y, Wang L, Jiao J, Hu Y, Lan X, Hou J, Li Y, Lu D. Sequential gastrodin release PU/n-HA composite scaffolds reprogram macrophages for improved osteogenesis and angiogenesis. Bioact Mater. 2023;19:24–37.
71. Chen W, Xie G, Lu Y, Wang J, Feng B, Wang Q, Xu K, Bao J. An improved osseointegration of metal implants by pitavastatin loaded multilayer films with osteogenic and angiogenic properties. Biomaterials. 2022;280: 121260.
72. Feng Q, Fatima K, Yang A, Li C, Chen S, Yang G, Zhou X, He C. Multi-modal imaging for dynamic visualization of osteogenesis and implant degradation in 3D bioprinted scaffolds. Bioact Mater. 2024;37:119–31.
73. Li Z, He D, Guo B, Wang Z, Yu H, Wang Y, Jin S, Yu M, Zhu L, Chen L, et al. Self-promoted electroactive biomimetic mineralized scaffolds for bacteria-infected bone regeneration. Nat Commun. 2023;14:6963.
74. Wang N. Instant integrin mechanosensing. Nat Mater. 2017;16:1173–4.
75. Chiu L-H, Lai W-FT, Chang S-F, Wong C-C, Fan C-Y, Fang C-L, Tsai Y-H. The effect of type II collagen on MSC osteogenic differentiation and bone defect repair. Biomaterials. 2014;35:2680–91.
76. Etich J, Rehberg M, Eckes B, Sengle G, Semler O, Zaucke F. Signaling pathways affected by mutations causing osteogenesis imperfecta. Cell Signal. 2020;76: 109789.
77. Hamidouche Z, Fromigue O, Ringe J, Haupl T, Vaudin P, Srouji S, Livne E, Marie PJ. Priming integrin alpha5 promotes human mesenchymal stromal cell osteoblast differentiation and osteogenesis. Bone. 2009;44:S218–9.
78. Wang Q, Wei Y, Yin X, Zhan G, Cao X, Gao H. Engineered PVDF/PLCL/PEDOT dual electroactive nerve conduit to mediate peripheral nerve regeneration by modulating the immune microenvironment. Adv Funct Mater. 2024;34:2400217.
79. Sun J, Zhao D, Wang Y, Chen P, Xu C, Lei H, Wo K, Zhang J, Wang J, Yang C, et al. Temporal immunomodulation via wireless programmed electric cues achieves optimized diabetic bone regeneration. ACS Nano. 2023;17:22830–43.
80. Lin Z, Shen D, Zhou W, Zheng Y, Kong T, Liu X, Wu S, Chu PK, Zhao Y, Wu J, et al. Regulation of extracellular bioactive cations in bone tissue microenvironment induces favorable osteoimmune conditions to accelerate in situ bone regeneration. Bioact Mater. 2021;6:2315–30.
81. Wang H, Hsu JC, Song W, Lan X, Cai W, Ni D. Nanorepair medicine for treatment of organ injury. Nat Sci Rev. 2024;11: nwae280.

Publisher's Note